ETH
Eidgenössische Technische Hochschule Zürich
Swiss Federal Institute of Technology Zurich

Improved Laser Scanning Microscopy Method and characterization of annular Lumped element resonators

Semester Thesis

Chun Tat Ngai and Oscar Bettermann

Nov 8th, 2016

Supervisor: Dr. Anton Potočnik

Group leader: Prof. Andreas Wallraff

Group: Quantum Device Lab, ETH Zürich

Abstract

Photo response (PR) is a photo-induced change of microwave response caused by illumination of a superconductor with laser beam, breaking Cooper pairs locally, thereby inducing change in kinetic inductance and resistivity of the resonators. Here, we investigate the PR dependence of niobium lumped element resonators using Laser Scanning Microscopy (LSM) technique and improve the spatial dependent measurement with Labview automatization. To examine the performance of this software, microwave and laser power dependence study of the PR were studied for a weakly coupled single lumped LC resonator. In addition, the change of resonance frequency and hence the current density of the strongly coupled annular structure was studied for each of its inductor and compared against a simple model. The corresponding measurements show that the new software provides a quick and reliable method to detect small changes in intrinsic loss and resonant frequency against laser position.

Contents

Chapter 1

Introduction

Since the advent of quantum theory in the early 20th century, scientists continued to develop deeper understanding of the fundamental weirdness of quantum mechanics. Meanwhile, large research effort is contributed to harness quantum resources to realise practical applications, for instance, quantum sensing, quantum cryptography and quantum computation [1]. Amongst these applications, quantum computation has always been one of the most important goal as it holds the key to understand many important physical and global problems in our ever-changing world. In computational complexity theory, many believed that quantum computing provides a "quantum speed up" in terms of computational efficiency over classical Turing machine to solve specific problems. One example is quantum simulation, an idea first proposed by Feynman [2] back in 1980s at Caltech, exponentially large Hilbert space of a quantum simulator would naturally allow a direct emulation of quantum systems. Today, there exists many promising architectures to realise quantum simulation, such as superconducting circuits, ion traps and cold atoms. However, before one can competently exploit these quantum systems to tackle sophisticated physical problem, precise and mature control of such system is indispensable.

Here, we explore a minimal version of such simulator of a superconducting lumped annular structure. We adopt the Laser Scanning Microscopy (LSM) technique to perform control and tuning of our quantum system. LSM was first introduced by Culbertson in 1993 [3] for probing the current density distribution of superconducting microstrip, using the fact that photo induced changes are proportional to the square of the local current density below the laser probe [4]. Important applications were found in detecting spurious modes from fabricated sample, X-ray from celestial bodies [5]. Moreover, superconducting structures are highly sensitive kinetic inductance detector, thanks to the dependence on the density of Cooper pairs. Later, Zhuravel [6]

developed methods to extract local resistivity and reactive from the photo-induced change of the microwave signal. Their work motivated a recent master thesis by Chen [7] exploring the photo response dependence of linear lumped element resonators at 4 K using LSM technique. In addition to the measurement capabilities of LSM, this technique could also be extended to detect photon response at the quantum limited microwave power regime, and reliably tuning resonance frequency of quantum system using laser probe, which could potentially solve the difficulty in the scaling of quantum integrated circuit. However, we wish to explore the system at a classical limited microwave, and study resonators connected in a circular boundary condition at Helium temperature, to understand other important effects, meanwhile, keeping our mindset open to the above possibilities.

This work begins with a beam calibration and Labview automization of the PR measurement procedure, to optimize the spatial dependent measurement. The software was further characterised by measuring the photo response dependence on laser and microwave power using 1 μm weakly coupled monomer. We then investigate the change in resonance frequency of an annular 4 resonators structure, and compare against a simple theoretical model. From the result, we observe some qualitative agreement between experiment and model. Nevertheless, the method permits sensitive detection of very small changes in resonator properties and opens door to study more complex resonator structures.

Chapter 2

Theory of photo response

In this section, we review the basic concepts of the photo response and superconducting lumped element resonator, followed by the second quantization description of a simplified Hamiltonian model. This allows one to make qualitative prediction of the influence of laser impinging on the superconducting resonators.

2.1 Superconductivity and photo response

In superconductors, there exists two types of charge carriers. The first kind is the Cooper pairs, formed by pairs of free electrons binding together indirectly by the electron-phonon interaction. These bosonic-like Cooper pairs can condense in a superconducting state where current can flow dissipationless below the critical temperature, T_c. The other kind is the quasiparticles, which dissipate energy due to scattering with phonons. When illuminating a superconductor with a laser beam, deposited energy indirectly breaks Cooper pairs into quasiparticles [8]. More specifically, if the energy of the optical photon is larger than 10Δ, where Δ is the superconducting gap, photons do not break Cooper pairs directly, instead their energy generate phonons, which then break Cooper pairs. As a result, the change in number density of Cooper pairs, enhances both the local resistivity R^* and the kinetic inductance L_{kin} of the superconductor. These effects lead to the change of resonant frequency and the internal loss of the resonator, given by eq. (2.5) and eq. (2.6). To further justify these relations, we shall briefly look at a simple resonator circuit (without feed line) in fig. 2.1. The equation of motion of this circuit can be derived by first invoking the Kirchhoff voltage law under energy conservation. This means that the sum of the voltage drops along any close loop equals to zero.

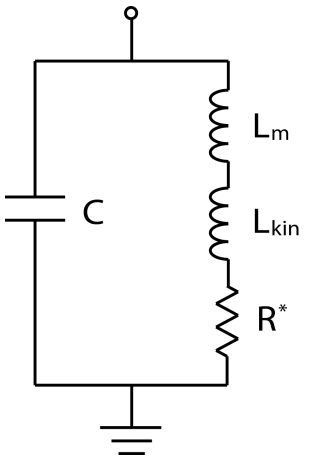

Figure 2.1: The circuit model of a superconducting lumped element LC resonator. C is capacitance, L_m is magnetic inductance, L_{kin} is kinetic inductance, and R^* is effective resistance given by two-fluid model. [7]

We obtain a voltage equation:

$$V_C + V_{L_m} + V_{L_{kin}} + V_{R^*} = 0 \tag{2.1}$$

By substituting the constitution relations $V_C = Q/C$, $V_{L_m} = L_m \dot{I}$, $V_{L_{kin}} = L_{kin}\dot{I}$, and $V_{R^*} = R^* I$, we have

$$\frac{Q}{C} + L_m \dot{I} + L_{kin}\dot{I} + R^* I = 0 \tag{2.2}$$

Taking derivative with respect to time, we get a second order equation of motion for the current:

$$\ddot{I} + \frac{R^*}{L_m + L_{kin}}\dot{I} + \frac{1}{(L_m + L_{kin})C} I = \ddot{I} + \gamma \dot{I} + \omega_0^2 I = 0\,. \tag{2.3}$$

By comparing the coefficient of the above equation, we obtained the dependence of two important physical quantities, the internal loss $\gamma = \frac{R^*}{L_m + L_{kin}}$ and the resonant frequency $\nu_0 = \frac{\omega_0}{2\pi} = \frac{1}{2\pi\sqrt{LC}}$ relating to the inductance. [1] We can derive the relationship eq. (2.5) as a simple demonstration. More

[1]The inductance comprises of contribution from both the magnetic and kinetic inductance $L = L_m + L_{kin}$. Magnetic inductance determines the amount of energy stored in magnetic field, whereas, kinetic inductance quantifies the amount of energy stored in the movement of the charge carriers, the role of L_{kin} is more prominent in particular for high frequency (GHz) alternating current in thin film superconductor. Both effects depend on the geometry of the superconductor.

rigorous treatment can be found in J. Chen's thesis [7]. Under small laser perturbation, $L_{kin} \rightarrow L_{kin} + \Delta L_{kin}$, given that $L_{kin} \propto n_s^{-1/2}$ [7], where n_s is number density of superconducting electrons

$$\begin{aligned} \Delta\omega_0 &= \frac{1}{\sqrt{(L_m + L_{kin} + \Delta L_{kin})C}} - \frac{1}{\sqrt{(L_m + L_{kin})C}} \\ &= \frac{1}{\sqrt{(L_m + L_{kin})C}}\left(-\frac{\Delta L_{kin}}{2(L_m + L_{kin})}\right) \end{aligned} \tag{2.4}$$

Similar argument holds for γ, leading to eq. (2.6). Hence, under small laser perturbation, ΔL_{kin} and ΔR^* are directly proportional to the laser power but independent of microwave power as one might intuitively expect, these results remain accurate in a regime where only small number of Cooper pairs is broken.

$$\Delta\nu_0 = -\frac{1}{4\pi\sqrt{C}}\frac{\Delta L_{kin}}{(L_m + L_{kin})^{3/2}} \tag{2.5}$$

$$\Delta\gamma = \frac{\Delta R^*}{L_m + L_{kin}} \tag{2.6}$$

In order to measure the change in reflection from the sample, we introduce the reflection coefficient Γ, which describes the ratio between the reflected voltage from the sample and the input voltage of the microwave signal $\frac{V_{out}}{V_{in}}$. In general, the reflection coefficient is a complex number and it holds all the physical information to characterise a resonator. It is conveniently visualised on an IQ plane as shown in fig. 2.3. Alternatively, the absolute magnitude $|\Gamma|$ and phase ϕ can be plotted against frequency in fig. 2.2, carrying the same information. To sum up, if a laser illuminates the resonator, we expect the decrease of resonant frequency and increase of internal loss, and the photo-induced change can be easily observed by measuring the reflection coefficient.

With all the ingredients, one possible definition of the photo response is given in eq. (2.9) as the change of the microwave resonator reflection coefficient after the laser is turned on. Here, we calculate the photo response by the difference of the reflection coefficient with laser off eq. (2.7) and laser on eq. (2.8). And the $|PR|$ can be shown to be proportional to the current distribution in the resonator circuit, which allows the characterisation of the superconductors [4].

$$\Gamma_{\text{LaserOff}}(\nu) = \frac{\kappa}{\frac{\gamma+\kappa}{2} + 2\pi i(\nu - \nu_0)} - 1, \tag{2.7}$$

where ν_0 is the resonance frequency, κ the external loss rate and γ the internal loss rate.

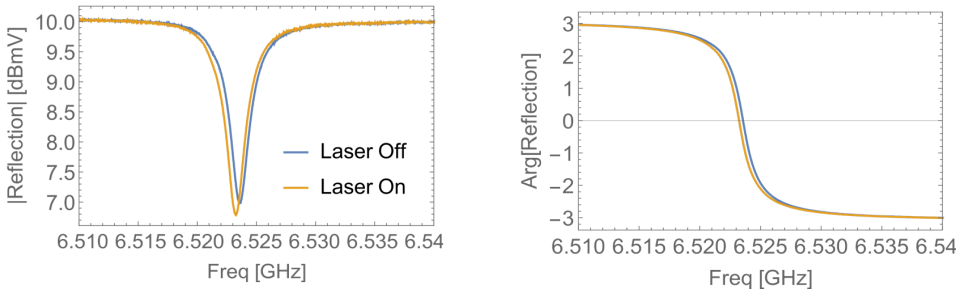

Figure 2.2: Change of reflected microwave signal induced by laser impinging on microwave resonator. When the laser is turned on, the resonance frequency of the resonator decreases and the linewidth is broaden.

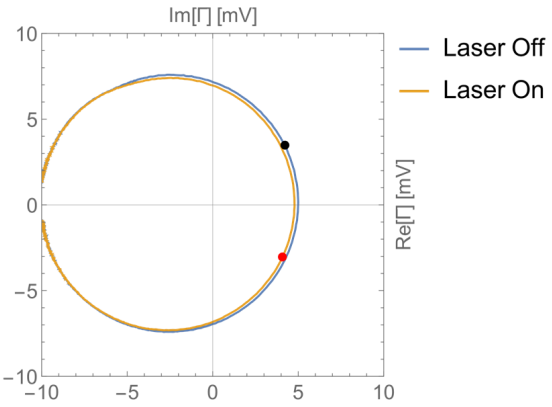

Figure 2.3: Visualisation of the complex reflection coefficient before and after turning on the laser on an IQ plane. The two points showed two IQ points as a complex conjugate pair, with the same absolute reflection coefficient, with the opposite sign in phase.

$$\Gamma_{\text{LaserOn}}(\nu) = \frac{\kappa}{\frac{\gamma+\delta\gamma+\kappa}{2} + i2\pi(\nu - \nu_0 - \delta\nu)} - 1, \tag{2.8}$$

where $\delta\gamma$ is change in the internal loss rate and $\delta\nu$ is the change in resonance frequency.

$$PR = \Gamma_{\text{LaserOn}} - \Gamma_{\text{LaserOff}}. \tag{2.9}$$

The change in $\delta\nu_0$ and $\delta\gamma$ are thus encoded in the complex reflection coefficient, which can be extracted with different methods that will be explained in a later section.

2.2 Introduction to lumped element resonators

Any physical circuit can be discretized into a network of lumped elements on condition that the length of the element is much shorter compared to the microwave wavelength $L \ll \lambda$. With the lumped element model, the attributes of the circuit can be treated as concentrated idealized electrical components such as capacitors and inductors connected by perfectly conducting lead wires. The EM field over the resonator can be seen as a constant with the long-wavelength approximation. An example of the lumped circuit model used in this study is shown in fig. 2.4. Four RLC resonators are connected in a periodic boundary fashion, coupled via coupling capacitors C_{Ji}. In order to measure the change in the resonator properties, a transmission line coupled via C_κ is used to send microwave photon into the circuit and reflected back.

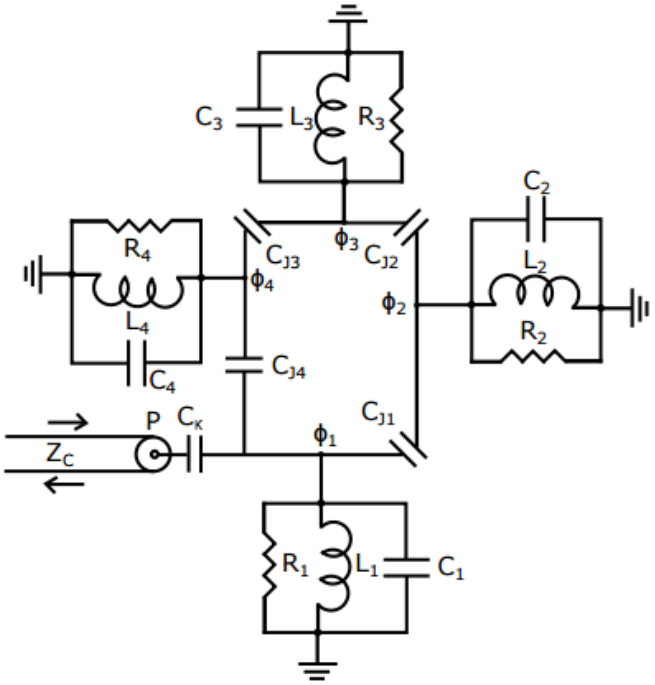

Figure 2.4: Circuit representation of the circular structure, consists of 4 individual lumped LC resonators with inductance L_i and C_i coupled via C_{Ji} in a circular boundary condition. The internal loss rate and external loss rate are captured by R_i and C_κ respectively via the transmission line P [9]

.

2.3 Hamiltonian in Second Quantization

Using the second quantisation formalism [9], the system properties are readily captured by the Lagrangian of the system, in turn providing a qualitative picture for the system response. Following the general recipe for circuit quantisation [10], we write down the Lagrangian of a general N coupled parallel LC circuits, where the effect of internal resistance R_i and external dissipation to transmission line resonator C_κ are not included.

Using the flux nodes representation, ϕ_i as coordinates [11]

$$\mathcal{L} = \frac{1}{2}\sum_{i=1}^{N} C_i \dot{\phi}_i^2 - \frac{1}{2}\sum_{i=1}^{N} \frac{\phi_i^2}{L_i} + \frac{1}{2}\sum_{i=1}^{N} C_{Ji}\left(\dot{\phi}_{i+1} - \dot{\phi}_i\right)^2 \tag{2.10}$$

with the periodic boundary condition for annular structure

$$\dot{\phi}_1 = \dot{\phi}_{N+1} \tag{2.11}$$

The above can be expressed in vector form as

$$\mathcal{L} = \frac{1}{2}\dot{\Phi}^T \underline{C}\dot{\Phi} - \frac{1}{2}\Phi^T \underline{L}^{-1}\Phi \tag{2.12}$$

with $\Phi = (\phi_1, \phi_2, ..., \phi_N)$ a column vector of flux nodes, $\underline{L}$ a diagonal matrix of inductances, and $\underline{C}$ the sum of the tridiagonal capacitance terms and the two extremal off diagonal capacitance terms. Where the tridiagonal terms originate from the coupling between nearest resonators linearly, and the extremal off diagonal terms describe coupling in a periodic condition. Performing the Legendre transformation, with the canonical conjugate momentum $q_i \equiv \frac{\partial \mathcal{L}}{\partial \dot{\phi}_i} = C_{ij}\dot{\phi}_j$ to obtain the Hamiltonian in matrix form

$$\mathcal{H} = \frac{1}{2}Q^T \underline{C}^{-1} Q + \frac{1}{2}\Phi^T \underline{L}^{-1}\Phi \tag{2.13}$$

where we define the column vector $Q = (q_1, q_2, ..., q_N)$. To summarise, the circuit diagram above (see fig. 2.4), is now translated into a classical Hamiltonian. By imposing the canonical commutation relation $\left[\hat{q}_i, \hat{\phi}_j\right] = -i\hbar\delta_{ij}$, together with the defined creation and annihilation operators $\hat{a}_i^\dagger, \hat{a}_i$, and ignoring fast-rotating term, we obtain the Hamiltonian in the quantization form

$$\mathcal{H} = \sum_{i=1}^{N} \hbar\omega_i \hat{a}_i^\dagger \hat{a}_i + \sum_{\langle i,j\rangle} \hbar J_{ij}\left(\hat{a}_i^\dagger \hat{a}_j + \hat{a}_i \hat{a}_j^\dagger\right) \tag{2.14}$$

where $\omega_i = \sqrt{(C^{-1})_{ii}(L^{-1})_{ii}}$, $J_{ij} = \frac{(C^{-1})_{ij}}{2\sqrt{(C^{-1})_{ii}(C^{-1})_{jj}}}\sqrt{\omega_i\omega_j}$ and we have neglected the zero point energy. Moreover, the sum $\sum_{\langle i,j\rangle}$ avoids double counting as $J_{ij} = J_{ji}$. Note that extremal off diagonal coupling J_{14} term have

the same strength as nearest neighbour coupling due to periodic boundary condition.

To study the eigenvector and eigenvalues of the above expression, we can write the Hamiltonian for our annular system as $\mathcal{H} = \hbar A^\dagger \underline{H} A$ with $A = (\hat{a}_1, \hat{a}_2, \hat{a}_3, \hat{a}_4)$ a column vector, $A^\dagger = \left(\hat{a}_1^\dagger, \hat{a}_2^\dagger, \hat{a}_3^\dagger, \hat{a}_4^\dagger\right)$ a row vector and

$$\underline{H} = \begin{bmatrix} \omega_1 & J_{12} & J_{13} & J_{14} \\ J_{12} & \omega_2 & J_{23} & J_{24} \\ J_{13} & J_{23} & \omega_3 & J_{34} \\ J_{14} & J_{24} & J_{34} & \omega_4 \end{bmatrix} \tag{2.15}$$

Here, we simplify eq. (2.15) by ignoring the higher order coupling terms, such as J_{13} and J_{24}, then the expression eq. (2.16) was used to fit the experimental parameters ω_i and J_{ij} by matching the observed resonant frequency with the diagonalised Hamiltonian eigenvalues, to obtain a photo response prediction for each of its resonance.

$$\underline{H} = \begin{bmatrix} \omega_1 & J_{12} & 0 & J_{14} \\ J_{12} & \omega_2 & J_{23} & 0 \\ 0 & J_{23} & \omega_3 & J_{34} \\ J_{14} & 0 & J_{34} & \omega_4 \end{bmatrix} \tag{2.16}$$

2.4 Input-output Theory

In addition to the Hamiltonian of the resonator system, we proceed to include the internal losses and coupling to the transmission line resonator (environment). By introducing the Langevin equations , we can describe the non-unitary dynamics of the resonator [12]

$$\dot{\hat{a}}_i = -\frac{i}{\hbar}\left[\hat{a}_i, \mathcal{H}\right] - \frac{\kappa_i}{2}\hat{a}_i - \frac{\gamma_i}{2}\hat{a}_i + \sqrt{\kappa_i}\hat{a}_{\mathrm{in},i} \tag{2.17}$$

where the first term on the RHS is the unitary evolution of i_{th} resonator, the second term is the on-site extrinsic coupling to the transmission line, the third term is the internal loss of the i^{th} resonator, and the last term is the drive term acting at i^{th} resonator. The equation effectively represents the dynamics of a driven damped oscillator.

The last ingredient is to impose the input-output boundary condition eq. (2.18), which returns the the reflection coefficient. The input-output relation is defined as

$$\hat{a}_{in,i} + \hat{a}_{out,i} = \sqrt{\kappa_i}\hat{a}_i \tag{2.18}$$

which provides a link between the microwave input drive, the intrinsic loss and the LC resonator. Combining with the equation for calculating the scattering matrix S_{ij}, see eq. (2.20) we obtain the complex valued reflection coefficient.

$$S_{ij} = \frac{\hat{a}_{out,i}}{\hat{a}_{in,j}} = \frac{\sqrt{\kappa_i}\hat{a}_i - \hat{a}_{in,i}}{\hat{a}_{in,j}} \tag{2.19}$$

This scattering matrix computes the ratio of the reflected microwave signal from port when an input signal i is sent in port j, in this experiment, we measure S_{11}, as only the signal sent and reflected along the same transmission line see fig. 2.4. By assuming classical signal, we can replace the operator with a classical number, $\hat{a}_i(t) = a_i e^{-i\omega t}, \hat{a}_{in}(t) = a_{in}e^{-i\omega t}$, we recover the reflection coefficient in the case of S_{11} [7], [9].

$$S_{11} = \frac{\hat{a}_{out,1}}{\hat{a}_{in,1}} = \frac{\sqrt{\kappa}\hat{a}_1 - \hat{a}_{in,1}}{\hat{a}_{in,1}} = \frac{\kappa}{\frac{\gamma+\kappa}{2} + 2\pi i(\nu - \nu_0)} - 1, \tag{2.20}$$

where $\kappa = \kappa_1$, since only resonator 1 was connected to the transmission line.

2.5 Eigenvector and eigenvalue analysis

We have combined the Langevin equation with the input-output relation, the reflection coefficient $|\Gamma(\nu)|$ of the annular system can now be plotted to match the Eigenvalues of the Hamiltonian in eq. (2.15) (via diagonalisation) against the observed frequency in the experiment. In order to obtain prediction of the photo response of the annular system resonator, the eigenvectors were also calculated, where the modulus square of each component is directly proportional to the photo response of each resonator.

The absolute value of the reflection coefficient was plotted for two cases, in the case I, we have annular structure with resonator resonant frequencies $\nu_1 \neq \nu_{2,3,4}$. the system possesses reflection symmetry between resonators 1 and 3 and trivial 360 degree rotation symmetry. In fig. 2.5(a), the reflection coefficient of the first case was studied, only 3 resonances were found at ν_1 = 7.47 GHz, $\nu_{2,3}$ = 7.838 GHz and ν_4 = 8.161 GHz, indicating the presence of degeneracy modes. An intuitive explanation is to argue that in a highly symmetrical structure, it is necessary to possess degenerate modes that obey the same symmetry operation. In order to investigate how degeneracy arises, in case II, we investigate the disappearance of the degeneracy by deliberately breaking the symmetry, i.e. ν_1 = 7.492 GHz, ν_2 = 7.833 GHz, ν_3 = 7.847 GHz and ν_4 = 8.186 GHz, while all other parameters (J, κ, γ) were unchanged. In panel (c), since the symmetry was reduced (removed reflection symmetry), the degeneracy disappeared. To gain further insight into the

role of the symmetry in the system, the stationary states (eigenvectors) of the system were also studied in panel (b), (d) for case I and II respectively. We plotted the modulus square of the Eigenvector components corresponding to the position of each resonator. Note that in both the Eigenvector and Eigenvalues spectrum, the Roman numericals label the corresponding mode, increasing from the left to right for panel (a) and (c). For case I, we found that the mode (i), (iv) exhibits opposite trend for each resonator. More importantly, for the degenerate modes (ii) and (iii), we observed no photo response in the left, right resonators and bottom, top resonators, called dark modes, as these modes can not be excited at specific resonators. To explain this, it was proposed that [9] the dark modes could arise from interference effect, due to the symmetry of the annular structure, the microwave signals travelling from the bottom port see no difference in travelling clockwise and anticlockwise, causing the probability density of the field to interfere destructively at specific resonators. Once the symmetry is broken, as can be seen from panel (d), all four modes return non-zero photo response for each resonator. With the above observations, it led to the conclusion that both the degeneracy and dark signal only present under the mirror symmetry through resonators 1, 3. By performing the photo response measurements, it would provide us information about the symmetry of the system. Nevertheless, more rigorous study is required to explain the above reasoning fully.

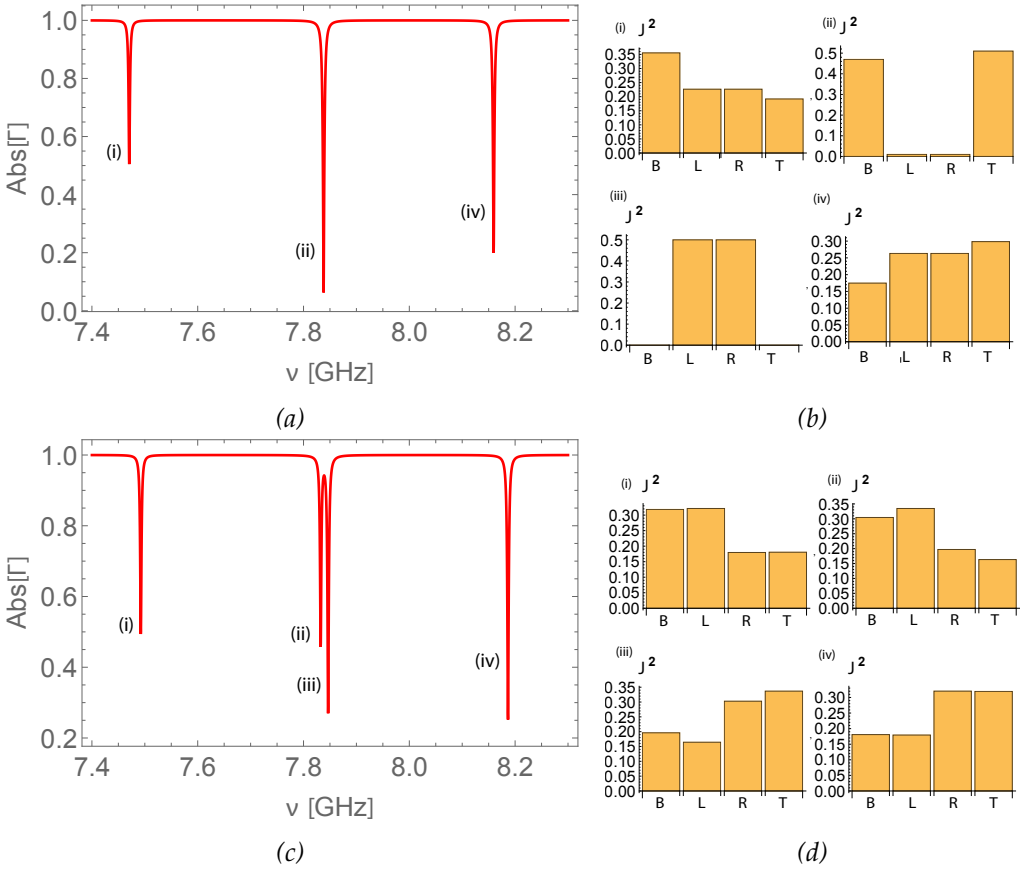

Figure 2.5: Absolute value of the reflection coefficients and eigenvectors for different annular systems. In the eigenvector plots each bar represents the current density (square of the eigenvector component) of a specific resonator, where, (R)ight , (B)ottom, (L)eft, (T)op correspond to the positions in the annular system. The eigenvectors are ordered according to the Roman numerical labels of the eigenvalues as shown in both the reflection coefficients and eigenvector plots. Panel (a),(c) show the absolute reflection coefficients with and without symmetry breaking respectively. We have taken guess parameters for panel (a): bare frequency $\nu_1 = 7.888$ GHz, $\nu_{2,3,4} = 7.79$ GHz, nearest neighbour coupling $J_{ij} = 0.17$ MHz, while for panel (c), $\nu_1 = 7.888$ GHz, $\nu_{2,3} = 7.79$ GHz, $\nu_4 = 7.79$ GHz, with ν_4 differs from ν_1, forcefully breaking the mirror symmetry between resonator 1, 4. The intrinsic $\gamma_i = 2.58$ MHz and extrinsic losses $\kappa = 4.85$ MHz. All the values were later found to match the experimental value on a qualitative level. Panel (b) and (d) show the eigenvectors of the Hamiltonian of this system with different symmetry. Dark modes were observed for the higher symmetric system.

Chapter 3

Setup

The experimental setup needed in order to investigate the photo response in lumped-element resonators has already been developed and used in previous work [7, 13]. The sample consists of multiple niobium-based superconducting lumped-element resonators and is placed in a high-vacuum fridge. In the frame of this thesis, a lumped single LC resonator (monomer) as well as the circular structure (tetramer) have been studied. The experimental setup consists of two parts, namely the optical and microwave part. The photo response can be detected by sending in a microwave signal and measure the reflected signal from the sample while being shined by a laser. Finally, a Labview program was created for the purpose of enabling accurate automatic measurements of the spatial dependence of the photo response. For a comprehensive description of the work that has been done to implement the latter, we refer to chapter 7.

3.1 The sample

The sample that was studied in this work is shown in figure 3.1. Measurements were performed on the monomer and the circular structure through port 9 and 7 as shown in fig. 3.2.

The sample is mounted on a printed circuit board, which provides the necessary connections between the resonators on the chip and the microwave equipment, shown in figure 3.3.

Since niobium is only superconducting at temperatures below $T_c \approx 9.2$ K, the sample must be mounted into a pulse tube-cooled fridge, which cools down the sample to 3 K. In order to avoid damage to components due to frozen air, the pressure in the fridge must be reduced before cooling down, reaching high vacuum of the order of 10^{-7} mbar.

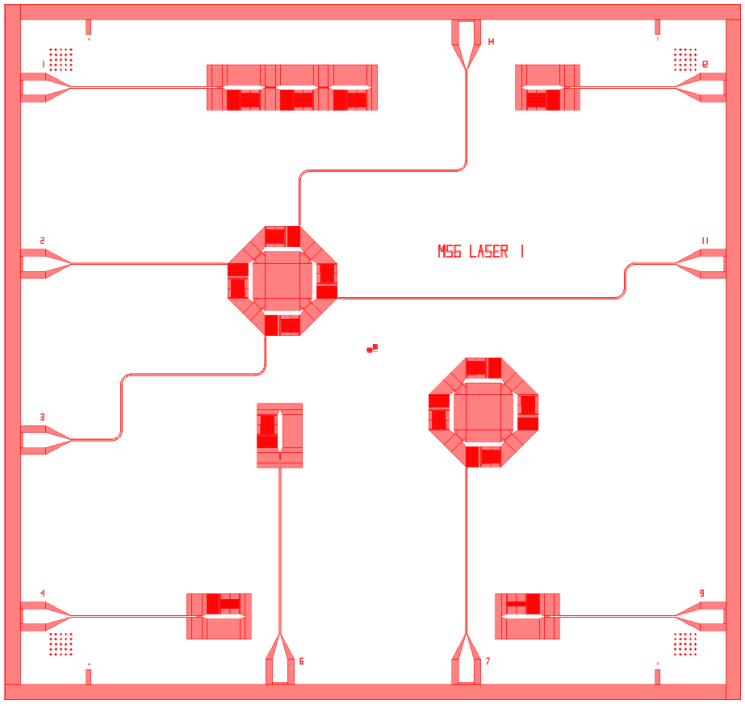

Figure 3.1: Sketch of the sample architecture. Port 7 leads to the asymmetric circular resonator with 3 µm wide inductor. Port 9 leads to the monomer resonator with 1 µm wide inductor.

3.2 Microwave setup

An overview of the microwave setup is shown on figure 3.4. The microwave signal is generated by two Rohde&Schwarz RF signal generators. The first RF signal is connected to the sample in the fridge. The incoming and reflected signals from the sample are split in two using directional couplers. The reflected signal is amplified first in the fridge at 3 K and after at room temperature and fed to the RF port of an IQ mixer. The amplified signal is down-converted and measured by either an Attocube Scanner Controller (ASC500) box or a field-programmable gate array (FPGA). The second RF signal is connected to the local oscillator (LO) port of the IQ mixer. There is a frequency difference Δf between the RF and the LO frequency. The second arm allows to keep a fixed phase relation between the LO and RF input into the IQ mixer by providing a phase reference. A constant phase relation is obtained by multiplying input A with the complex conjugate of input B into the FPGA.

The FPGA-based measurement device that has been used is based on a Virtex 6 FPGA. If using FPGA for data acquisition, as it has been the case in this thesis, a frequency difference (or intermediate frequency) of $\Delta f = 250$

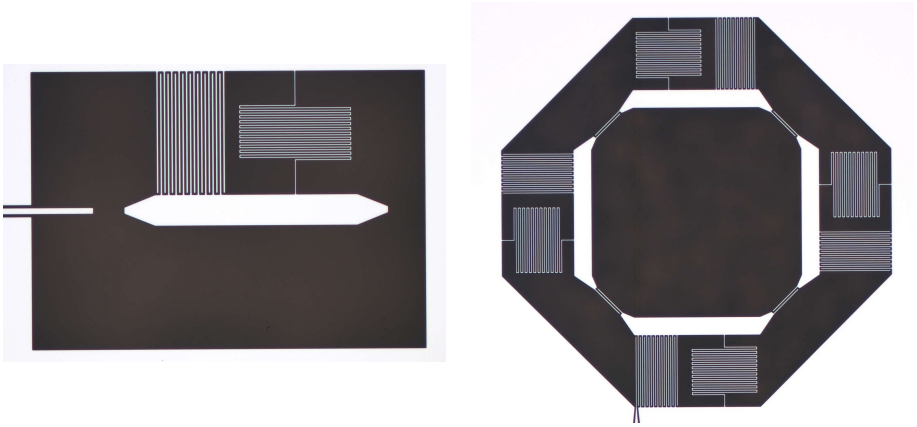

Figure 3.2: Lumped-element resonators on which measurements have been performed. The single resonator is shown on the left while the annular resonator is shown on the right. The pictures have been taken by Anton Potočnik.

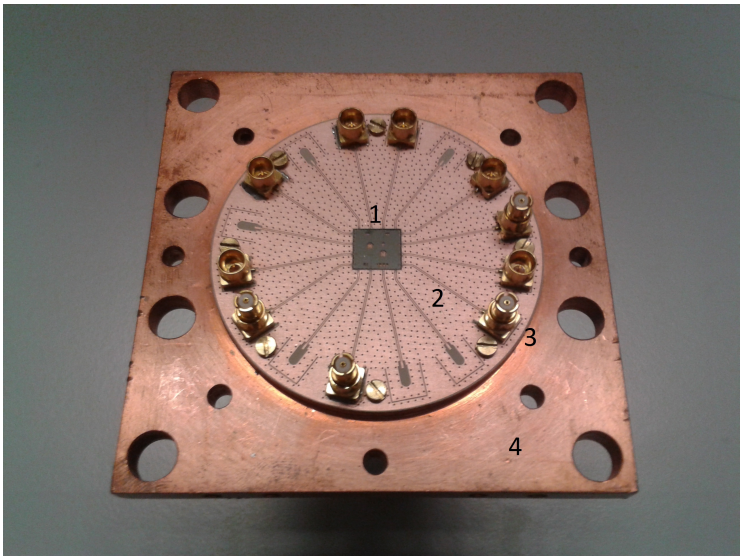

Figure 3.3: Photograph of the sample used in the experiment. The sample (1) is mounted in the center of a PCB chip (2). The feed lines of the resonators are connected to the SMP connectors at the edge of the PCB. Bullets (3) are mounted on the relevant connectors to enable the connection to the coaxial lines. The chip is screwed on a metallic plate (4), which is then mounted into the fridge.

MHz is used, which is then digitally down-converted to a DC signal. At the Qudev lab, a Labview software called Cleansweep allows to perform FPGA measurements[1].

[1]Cleansweep will be replaced in a close future by a new software called SweepSpot.

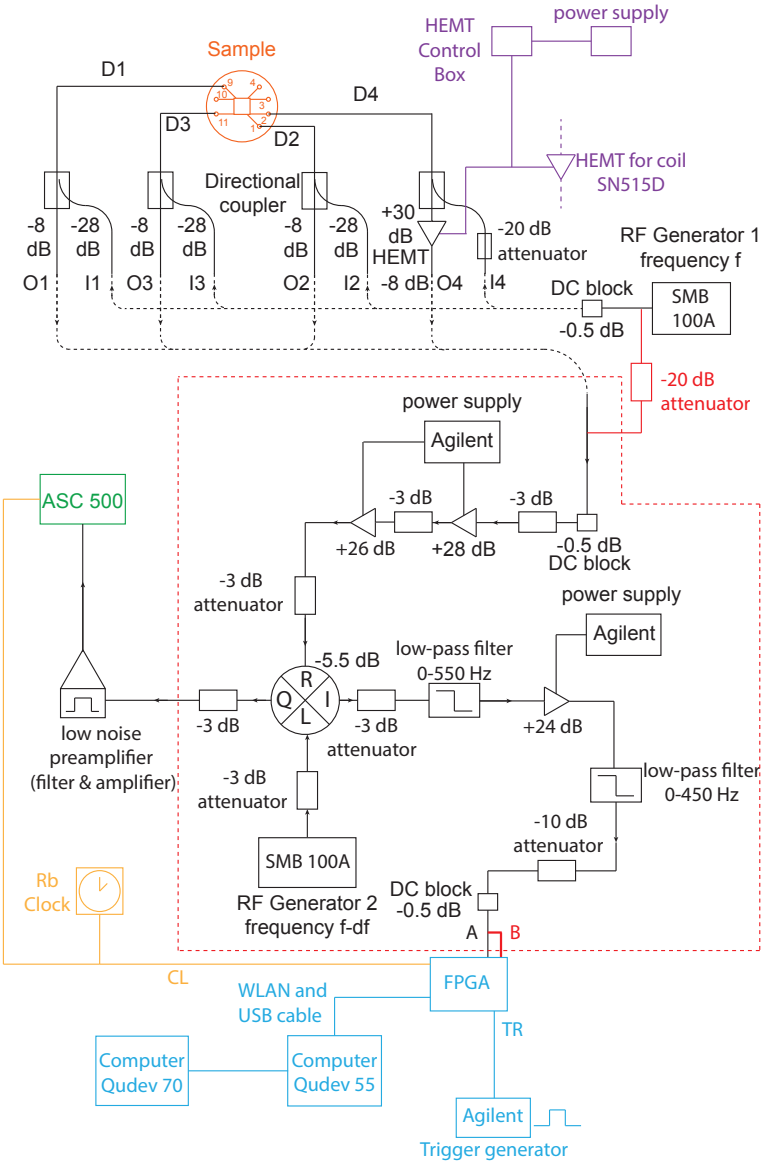

Figure 3.4: Schematics of the microwave setup, based on [13]. There are two arms such as the one located in the red box. The red elements denote alternative connections for the second arm. A -10dB attenuator has been added between the DC block and the 0-450 Hz low-pass filter on each arm in comparison with [13].

3.3 Optical setup

In order to generate the photo-response, photons must illuminate the resonators on the chip. In this experiment, we use a 405 nm laser shining on the chip that can be moved using Attocube positioners. This optical setup is also very useful to get optical images of the sample, which is necessary to determine the position of the laser with respect to the sample and enable shining exactly over the desired structure.

An overview of the optical setup is shown on figure 3.5. The diode laser beam is stabilized using acousto-optical modulators (AOM), selecting the first-order reflected beam, whose intensity can be modulated by the AOM input. It is then sent via an optical fiber onto a 90:10 beam-splitter. The transmitted beam is measured with a photodiode, and provides feedback to a PID controller that stabilizes the power of the diffracted beam by controlling the AOM input. The reflected beam is sent via a fiber into the fridge, and shines on the sample through a confocal lens system. An Attocube piezoelectric positioning system allows to move the x, y and z position of the lens. The motion in x and y directions change the position of the laser over the sample and the motion in z direction allows to focus the laser beam. The reflected signal is attenuated and measured by a photodiode, and finally fed to the Attocube scanning controller. The ASC500, via the ANC350 piezo motion controller, perform the 2D scan over the sample. The scan can be performed by the user via a software controlling the ASC500, called Daisy.

There are two scanning modes in Daisy, called Scanner and Stepper, which concern different ranges of scans. The Stepper is conceived for large scans, over a range of 4 mm $\times$ 4 mm. This range is ideal to measure objects of the size of full resonators, and to roughly determine the position of the laser. The Scanner is designed for a maximal range of 30 μm $\times$ 30 μm at low temperatures, and is therefore useful to precisely resolve structures such as single conducting lines. This is the useful scanning process in order to precisely go through inductor lines with the laser to perform the photo-response measurements.

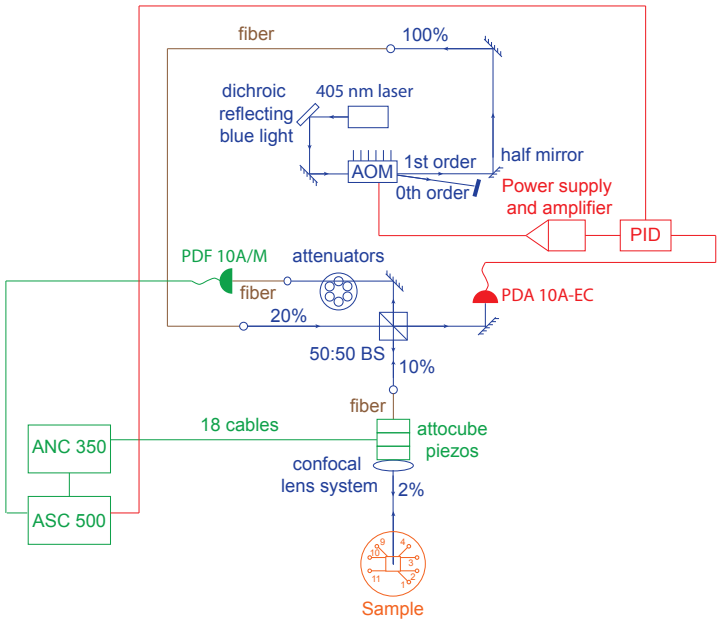

Figure 3.5: Diagram of the optical setup, based on [13].

Chapter 4

Measurement of the photo response

In the previous 2 sections, the theory of the photo response and the LSM setup were introduced. The vast functionality and flexibility of the ASC500 and the FPGA offer many approaches for photo response measurement. Two of these standard measurement techniques are discussed here. For more details of other experiment, one can refer to the last section in appendix (see section 7.3).

4.1 Measuring the photo response

In this section, we discuss several measurement approaches to measure the photo response. Each measurement method has its own advantage and disadvantage, depending on the type of parameters being measured.

4.1.1 FPGA Static photo response measurement

The static photo response method is the simplest but time costly way of measuring the photo response, one has to obtain the reflection coefficient measurement by sweeping through a given frequency range with both laser on and off. By fitting the complex reflection coefficient eq. (2.7) on a IQ plane, all the physical parameters can be retrieved. The downside of this approach is the long measurement time.

4.1.2 FPGA Single point photo response measurement

In a previous thesis [13], an improved method to measure the spatial dependence of the photo response was proposed, which provides a faster measurement method to extract change of the relevant resonator parameters i.e. $\delta\nu_0$ and $\delta\kappa$.

Recall that the reflection coefficient is given by

$$\Gamma_{\text{LaserOff}}(\nu) = \frac{\kappa}{\frac{\gamma+\kappa}{2} + 2\pi i(\nu - \nu_0)} - 1, \tag{4.1}$$

When one shines a laser on the resonator, the photons break Cooper pairs and a shift $\nu_0 \to \nu_0 + \delta\nu_0$ and $\gamma \to \gamma + \delta\gamma$ is observed. It was noticed that the function

$$f(\delta\nu_0, \delta\gamma) = \frac{1}{\Gamma_{\text{Laser On}} + 1} - \frac{1}{\Gamma_{\text{Laser Off}} + 1} = \frac{1}{\kappa}\left(\frac{\delta\gamma}{2} - i2\pi\delta\nu_0\right) \tag{4.2}$$

provides a very convenient way to get the change in the reflection coefficient parameters since $\delta\gamma = 2\kappa\Re(f)$ and $\delta\nu_0 = -\kappa\Im(f)/2\pi$, where $\Re(z)$ and $\Im(z)$ corresponds to the real and imaginary part of the complex number z, respectively.

Before one performs the spatial photo response measurement, the grid for measurement is first prepared by retrieving optical reflection of the inductor line using a scanner module called Pathmode Scanner that has been implemented in the frame of this thesis. Then, one performs a frequency sweep measurement against the reflected voltage, where we extract the resonance frequency ν_0 and the external loss rate κ for the photo response measurement. In theory, the measurement method only requires a single frequency, however, as pointed out by Samuel [13], typically the parameters were extracted at the resonance frequency ν_0 for the best signal-to-noise ratio. Upon retrieval of the resonant frequency, the spatial dependence of photo response can be obtained by setting the RF frequency to the resonant frequency, and then scan from a position far away from the inductor (corresponding to laser off) with the laser always turned on. Thanks to FPGA, with this Labview software, we can perform measurements with a high averaging of 262144 measurements per second in short period of time (7 minutes for 100 points across 2 μm region).

A more exhaustive description and manual of the Labview implementation can be found in section 7.2.

Chapter 5

Experimental results and discussion of the photo response measurement

5.1 Characterization

With the newly developed Labview software, the laser position can be swept as an additional sweeping parameter automatically within group software SweetSpot. To test the new method, we performed a microwave and laser power dependence of the change in the resonance frequency $\delta\nu_0$ and internal loss $\delta\gamma$ using a weakly coupled monomer with 1 μm wide inductor line. At the end, the $\delta\nu_0$ and $\delta\gamma$ of the strongly coupled annular structure with 3 μm wide inductor line were studied as a function of inductor position on the annular structure, and compared against a simple Hamiltonian mentioned in chapter 2. Note that the $\delta\nu_0$ and $\delta\gamma$ are directly proportional to the superconducting current density, which also provides one the probe for current distribution on the sample.

5.2 $\delta\nu_0$ and $\delta\gamma$ dependence on microwave power and laser power

Before one measures the microwave or laser dependence of $\delta\nu_0$ and $\delta\gamma$, the properties of the microwave resonators must be characterised. We start with the characterisation for microwave power, the resonant frequency ν_0 and the extrinsic loss κ do not change with microwave power, therefore, only a single reflection coefficient measurement with the laser off was measured and fitted at -116 dBm at roughly 3 K, see left figure on fig. 5.1. The resonant frequency ν_0 and κ were found to be 7.62392 GHz and 0.172587 MHz respectively. To obtain the reflection coefficient for other microwave powers, we simply measured the input voltage by sweeping through the reflected voltage signal against microwave power at an off-resonance frequency.

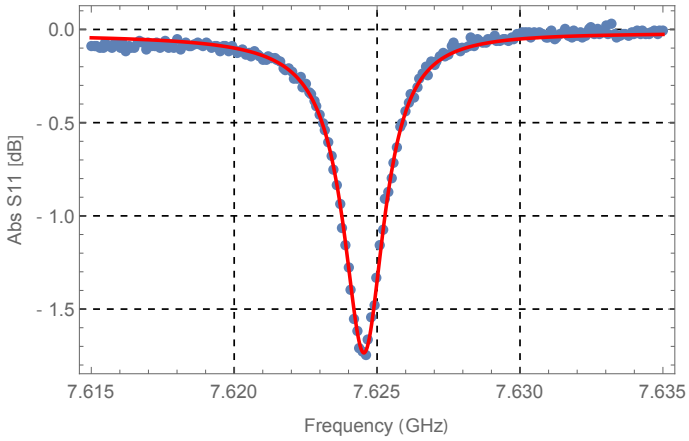

Figure 5.1: Reflection measurement with fitted resonance at -116 dBm with the laser turned off to extract κ and ν_0.

Similarly, in order to measure the laser power dependence, a dark measurement was done to characterise the resonator at microwave power of -116 dBm at 3.5 K. The ν_0 and κ were found to be 7.6184 GHz and 0.1786 MHz, the slight shift in both parameters compared to the values obtained for microwave characterisation are expected due to more Cooper pairs breaking at a higher temperature (3.5 K).

With the above characterisation for both dependence, we are ready to measure the spatial photo response using the new implemented Labview software. The Pathmode scanner was run to retrieve an optical image, which defines the range for the spatial PR measurement. Next, the laser is turned on and the laser position was chosen as a sweeping parameter, to retrieve spatial PR across a single inductor line.

Position dependence of $\Delta\nu_0$ and $\Delta\gamma$ with varying microwave power

The following measurements were performed at 3.0 K from -126 dBm to -111 dBm with $4.88\mu W$ laser power on the weakly coupled monomer of $1\mu m$ wide inductor line. In fig. 5.2(a), $\delta\nu_0$ is plotted against distance d above the inductor line. Initially, the laser was far away from the inductor line ("laser off"), no change in $\delta\nu_0$ was observed, the resonant frequency began to decrease when the laser approached the centre of the inductor line ("laser on"), and slowly recovered again as the laser moved away from the inductor line, which returns an overall symmetric line shape, coinciding with the shape of the inductor line strip. For clarity, only 3 microwave powers -125 dBm, -120 dBm and -118 dBm were shown. The maximum change of $-\delta\nu_0$ above the inductor line for each RF power was fitted against a gaussian function, from which the height of the dips were extracted and then plotted as a function

of the microwave power on the right figure in fig. 5.2(b). The uniform distribution of the $\delta\nu_0$ suggested that the resonant frequency is independent of microwave power, the result agrees with the prediction according to eq. (2.5).

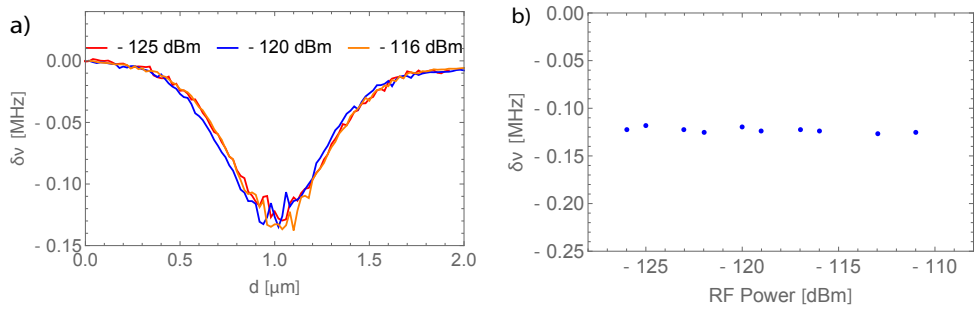

Figure 5.2: (a) Left: $\delta\nu_0$ against laser position d as a function of microwave power and laser power of 4.88 μW at the sample (b) Right: $\delta\nu_0$ against microwave power from -126 dBm to -111 dBm with laser power of 4.88 μW above the center of the inductor.

In fig. 5.3, the behavior was similar to $\delta\nu_0$ except that γ increases as the laser moves close to the inductor line as one would expect. However, unlike in the case of $\delta\nu_0$, the internal loss actually showed an increasing trend as a function of the microwave power. Note that the narrow line width of the monomer implies γ is more sensitive to change in number of Cooper pairs compared to the change in ν_0. Moreover, the strong focus of the laser beam onto the inductor line could lead to large number of Cooper pairs breaking locally, which leads to non-linear behavior from the linear theory in eq. (2.6), or this could also be affected by temperature drift from laser heating.

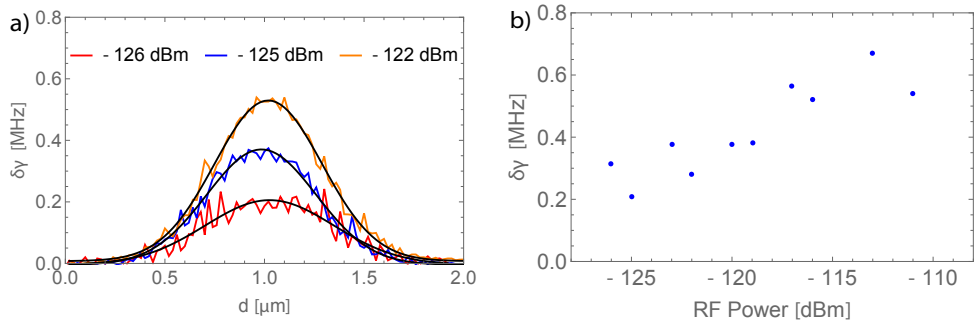

Figure 5.3: (a) Left: $\delta\gamma$ against laser position d as a function of microwave power and laser power of 4.88 μW at the sample (b) Right: $\delta\gamma$ against microwave power from -126 dBm to -111 dBm with laser power of 4.88 μW above the center of the inductor. An increasing trend of $\delta\gamma$ with increasing microwave power is observed.

Position dependence of $\Delta\nu_0$ and $\Delta\gamma$ with varying laser power

The laser power was varied from 0 μW to 10 μW at -116 dBm with a focused laser beam at 3.5 K. However, when the laser power was ramped up, the sample temperature becomes unstable due to laser heating. Therefore, the temperature was held at 3.5 K using the feedback control loop using a temperature controller. Note that the small inductor line width of weakly coupled monomer is expected to have very sensitive change in PR, this also implies any small unwanted thermal fluctuation could affect the result significantly.

Similar to the observation in microwave power, we observe decreasing and increasing trend for $\delta\nu_0$ and $\delta\gamma$ respectively around the center of the inductor line at approximately 0.7 μm. Larger photo-induced shift in $\delta\nu_0$ and $\delta\gamma$ were observed with increasing laser power as shown in figure (a) of fig. 5.4 and fig. 5.5. This behavior is expected as the number of Cooper pairs being broken increases with larger laser power, i.e. more photons are impinging onto the inductor. Nevertheless, in figure (b) of fig. 5.4 and fig. 5.5, both parameters exhibited exponential relationship with increasing laser power, this observation once again with the focused laser, the number of Cooper pairs being broken were probably too large to be considered in the linear laser power regime. To conclude, the laser dependence measurements show a good qualitative agreement of trend (i.e. ν_0 drops and γ increases with increasing laser power). However, both parameters $-\delta\nu_0$ and $\delta\gamma$ do not obey eq. (2.5) and eq. (2.6), a non-linear PR theory is required to explain the observed trend.

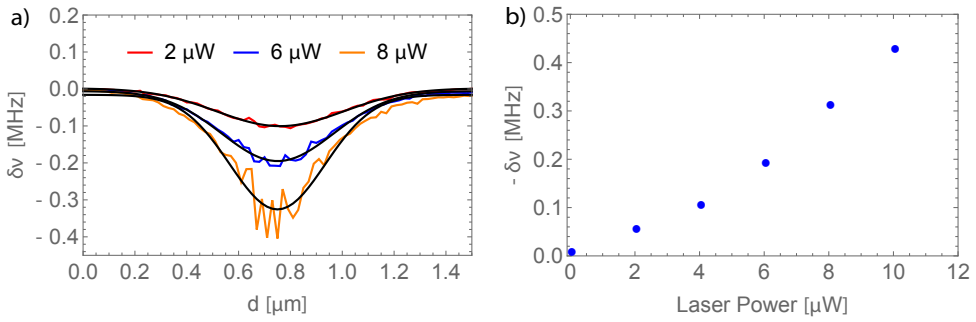

Figure 5.4: (a) Left: $\delta\nu_0$ against the laser position d as a function of laser power and microwave power of -116 dBm. (b) Right: $\delta\nu_0$ against laser power from 0 μW to 10 μW above the center of the inductor. The plot shows a non-linear dependence with increasing laser power.

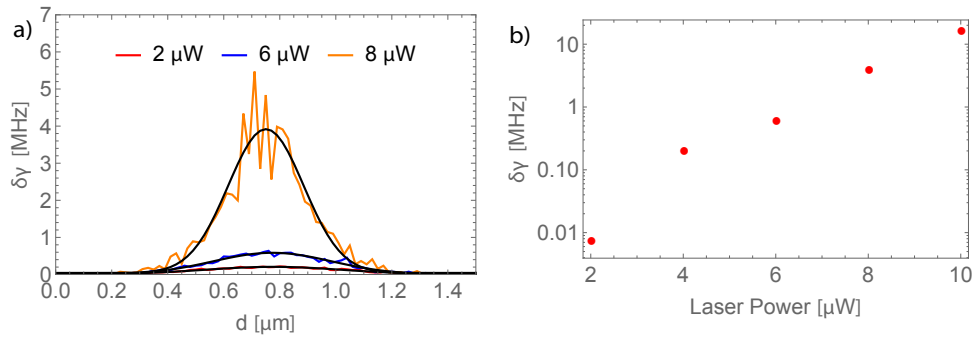

Figure 5.5: (a) Left: $\delta\gamma$ against the laser position d as a function of laser power and microwave power of -116 dBm. (b) Right: $\delta\gamma$ against laser power from 0 μW to 10 μW above the center of the inductor. The log plot shows an exponential trend of $\delta\gamma$ with increasing laser power.

5.3 Measuring resonances of the circular structure array

We now move on to the annular resonator connected to port 7 on figure 3.1. The goal is to measure the shift in resonance frequency $\delta\nu_0$, since it is directly linked to the current density J in the inductors through $\delta\nu_0 \propto J^2$ [4]. It is therefore interesting to compare $\delta\nu_0$ for several resonance frequencies of the circular structure in each of its inductors. First, we indeed need to find the resonances of the tetramer with a frequency scan. The spectrum of the circular structure is shown on figure fig. 5.6.

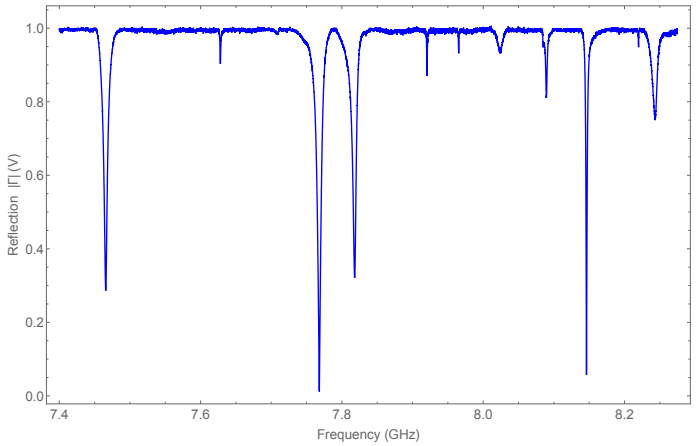

Figure 5.6: Full frequency sweep spectrum of the 3 μm inductor width circular structure. In this study, only 4 of the sharpest resonances were studied for their photo response.

In comparison with the monomer, where only one resonance frequency was

present, we here have several resonances. This is due to the fact that we now deal with four coupled resonators. In addition to the four expected resonance frequencies, we see a collection of additional modes, which can be explained by defects of the sample as well as parasitic coupling to other resonators. For instance, one of the additional modes can be strongly suspected to correspond to the resonance frequency of the single resonator that has been studied before. A reason for this is that by looking at figure 5.1, we see that the resonance frequency is about 7.6245 GHz. On figure 5.6, we see that there also is a dip at a frequency slightly below 7.625 GHz. Nevertheless, the reason why we cannot compare both measurements is that they have been performed at different temperatures, and the resonance frequencies are strongly temperature-dependant. A study should have been made at constant temperature to prove that we see the resonance frequency of the single resonator on the annular resonator spectrum. We have decided to study the four main resonance frequencies given in table 5.1 and indicated in figure 5.6.

Resonance 1	Resonance 2	Resonance 3	Resonance 4
7.4634 GHz	7.7671 GHz	7.81765 GHz	8.1454 GHz

Table 5.1: Frequency of the resonances of the circular structure that have been studied in this thesis. The frequencies have been measured at a temperature of 3.1 K.

We now proceed by showing and discussing $\delta\nu_0$ at each of the inductors for each resonance frequency[1]. Note that all measurements in this section have been performed with a laser power of 10 μW and a microwave power of -126 dBm. Since the resonator is asymmetric, we naturally expect to get different changes for each inductor, and to see the relation between them to change for different resonance frequencies.

The change in resonance frequency as a function of space at 7.4634 GHz and 7.7671 GHz is given on figure 5.7, at 7.81765 GHz and 8.1454 GHz on figure 5.8.

We see indeed that for each different inductor, the change of resonance frequency, which has the form of a convolution, is different. The trend changes for each resonance frequency, as expected by an asymmetric structure. We see for instance that the left inductor is in a "dark mode" at 7.81765 GHz, since there is no significant $\delta\nu_0$. This indicates that the current density is

[1]We do not discuss the change in internal loss rate $\delta\gamma$ here. Indeed, since the resonances are broad, a change of resonance frequency (hence of the phase of the photo-response) can be measured more sensitively than a change of internal loss rate (hence of the amplitude of the photo-response), and leads to a far better signal-to-noise ratio.

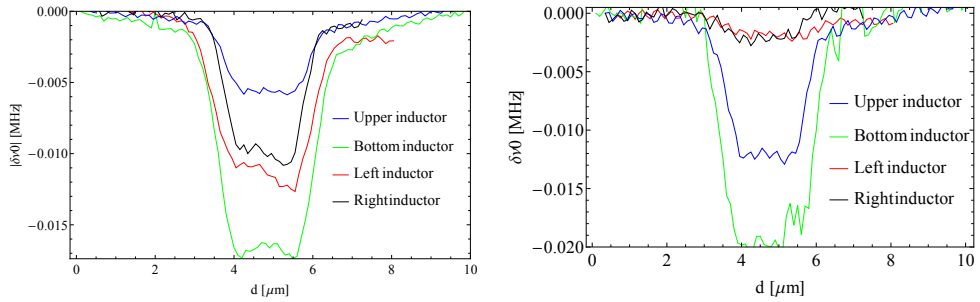

Figure 5.7: On the left figure, $\delta\nu_0$ at 7.4634 GHz. On the right figure, $\delta\nu_0$ at 7.7671 GHz. Both measurements have been taken at 3.1 K.

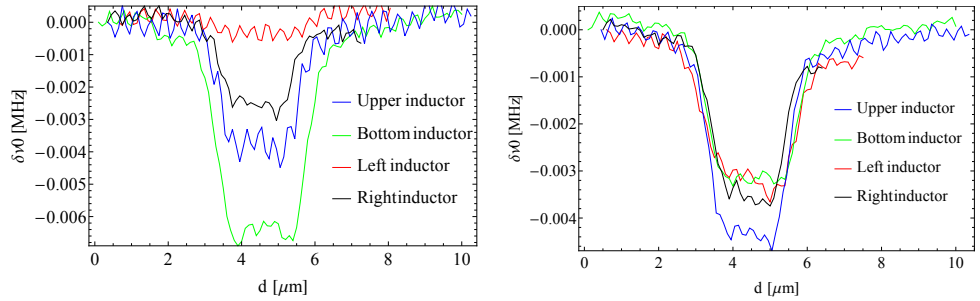

Figure 5.8: On the left figure, $\delta\nu_0$ at 7.81765 GHz. On the right figure, $\delta\nu_0$ at 8.1454 GHz. Both measurements have been taken at 3.1 K.

zero in this inductor at this given frequency. We verify that $\delta\nu_0$ is always negative.

In order to summarize our observations for the change of resonance frequency, a fit of the above functions has been performed and the height of the convolution extracted for each resonance frequency. The resulting amplitudes are then compared to the eigenvectors of the simple model in Hamiltonian formalism introduced in chapter 2, with the parameters adjusted to best match our data. The resulting plots are shown in figures 5.9, 5.10, 5.11 and 5.12. This confirms the observation of different photo-response amplitudes for different frequencies and inductors.

The experimental data does not seem to match the theoretical model. Indeed, on figures 5.9, 5.11 and 5.12, it is possible to see at least some qualitative agreement between experiment and theory, but on figure 5.10 we see a very different behaviour than theoretically expected. This can be explained by different factors, such as defects in our sample, parasitic effects due to other resonators on the same chip, or maybe the fact that the theoretical model used is too simple for our system. As a conclusion of this part, however, we see that other measurements on a new sample, perhaps isolated on the chip,

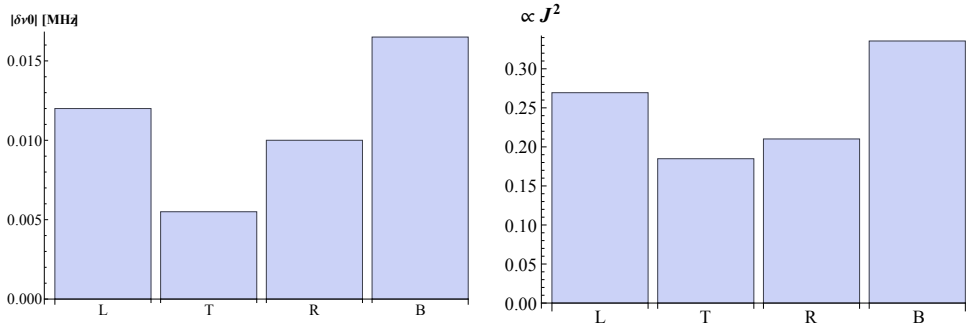

Figure 5.9: On the left, bar plot of $\delta\nu_0$ for a laser on the inductor line extracted from a fit, at 7.4634 GHz. On the right, theoretical fit for the current density.

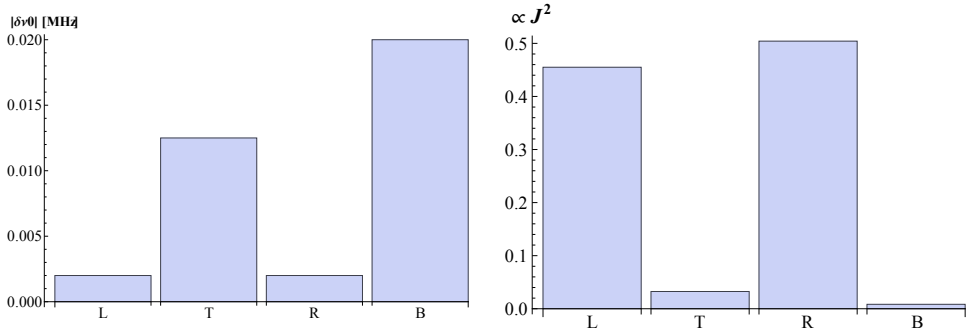

Figure 5.10: On the left, bar plot of $\delta\nu_0$ for a laser on the inductor line extracted from a fit, at 7.7671 GHz. On the right, theoretical fit for the current density.

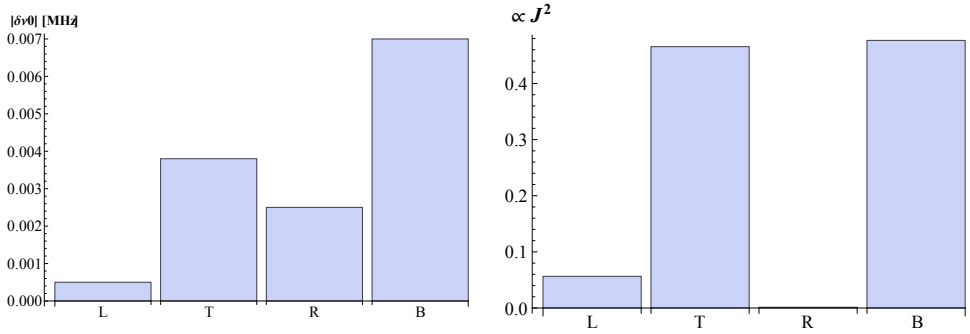

Figure 5.11: On the left, bar plot of $\delta\nu_0$ for a laser on the inductor line extracted from a fit, at 7.81765 GHz. On the right, theoretical fit for the current density.

should be performed to reach qualitative conclusions.

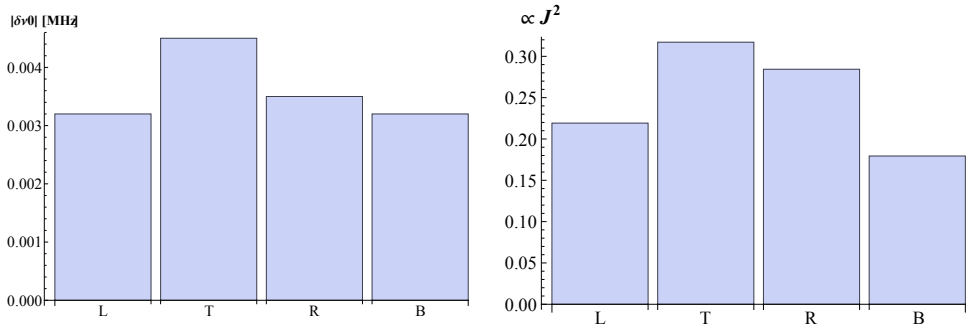

Figure 5.12: On the left, bar plot of $\delta\nu_0$ for a laser on the inductor line extracted from a fit, at 8.1454 GHz. On the right, theoretical fit for the current density.

Chapter 6

Summary and Conclusion

In this thesis, we have investigated the laser-induced photo-response of niobium-based lumped-element LC resonators, following previous work on the same setup by J. Chen [7] and S. Gyger [13]. The single-point measurement technique introduced by the latter has been used and improved thanks to an automatization of the measurement process.

After an introduction to the subject and to the basic theory of the photo-response in superconducting circuits in chapters 1 and 2, we detailed the setup that has been used to perform the measurements in chapter 3. Since the setup is almost unchanged with respect to the one that has been used in [13], the only specificities to this thesis are the sample that has been used and some minor changes to the setup. Furthermore, in chapter 4 we explained the single-point measurement technique introduced in [13]. We also explained how it has been improved by the conception of a Labview software that moves automatically the laser in order to measure how the photo-response evolves as a function of the position of the laser. In other words, this allows to measure the spatial dependence of the photo-response.

We then were ready to perform several measurements, whose outcomes are given in chapter 5. Two distinctive directions have been investigated:

1. In section 5.2, we focused on the photo-response of a 1 μm monomer resonator. The goal was to look at the change in resonance frequency $\delta\nu_0$ and internal loss rate $\delta\gamma$ as a function of the microwave (MW) power and of the laser power. It turned out that both $\delta\nu_0$ and $\delta\gamma$ are independent of the MW power as predicted from theory. The behaviour is quite different if we look at the laser power. Since the laser breaks Cooper pairs, $\delta\nu_0$ and $\delta\gamma$ were expected to strongly depend on the laser power. Indeed, we observed an exponential growth of $-\delta\nu_0$ and $\delta\gamma$ for increasing laser power, which differs from the theoretical prediction.
2. Finally, we investigated in section 5.3 the change in resonance fre-

quency $\delta\nu_0$ of the different inductors of the 3 μm circular structure at different resonance frequencies. Since it is composed of four coupled single resonators, four resonance frequencies were expected, and many more were indeed measured. In particular, $\delta\nu_0$ can be directly related to the current density in the inductor. Since the resonator has an asymmetric configuration, different amplitudes were expected at the different resonators, with changing relations at different resonance frequencies. We indeed observed such an asymmetry when comparing the amplitudes of the photo-response at all four inductors. For one resonance frequency, we could also observe a so-called dark mode, which means that there was a zero current density in one inductor. Nevertheless, we could not make our experimental results agree with a simple theoretical model, which suggests that the measurements need to be retaken on a new sample.

As a conclusion of this part of the thesis, we can say that the single-point measurement technique combined with the automatization of the measurement process allowed us to perform a very precise and fast measurement of the photo-response as a function of the laser position, at a resolution that could not be reached until now on this setup. In particular, we could observe with a very good precision the current density profile inside conducting lines. We could indeed see that there were no "edge effects", the current distribution has a profile of a simple convolution between a rectangle and a Gaussian. By fitting the curve obtained, we could extract with a very good precision quantities such as the change in resonance frequency or internal loss rate.

In chapter 7, we finally treat two additional points. First, we calibrate the spot size of the laser which was used in the experiments. Then, we give a complete explanation of the implementation of several Labview Virtual Instruments (VIs) to automatize the measurement process. In particular, the interested reader will find there all useful information to use the so-called Pathmode scanner, which encapsulates the step-by-step position scanning process that has been used. This process has been included in a software called SweepSpot, which now allows to properly perform a scan over different laser positions. All informations about how to use this new functionality in this software can also be found in this chapter.

Chapter 7

Appendix

7.1 Calibration of laser beam width and ASC500 step size

In LSM, the laser beam spot size defines the resolution of the scan. The beam spot size was calibrated against the reference test structure with well-determined width, see fig. 7.1.

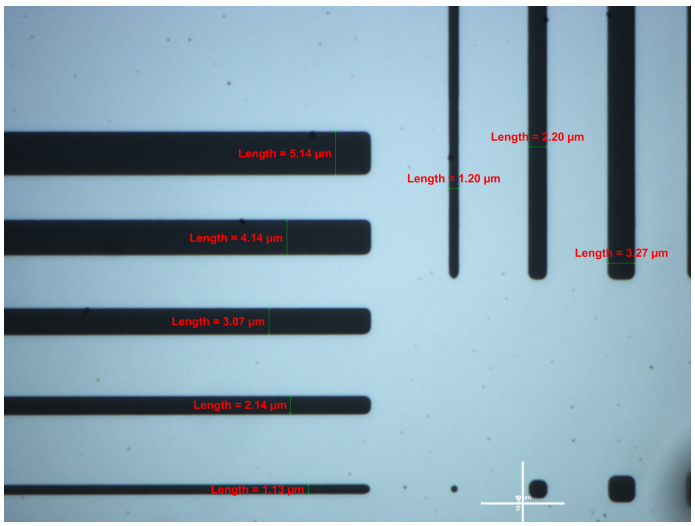

Figure 7.1: Test structure with high precision measured width

The calibration is done by step scanning both the horizontal and vertical test structures along vertical and horizontal direction respectively with a focused beam in 3 K. Each of the test structure strip was fitted by a convolution of a rectangular function and the gaussian function. As an example, we show

reflected laser intensity scanning over a 1 μm wide test structure line, shown in fig. 7.2. By plotting the fitted rectangular width against the test structure width, the calibrated step size per pixel (gradient) can be obtained from a line of best fit through 5 data points, see fig. 7.3.

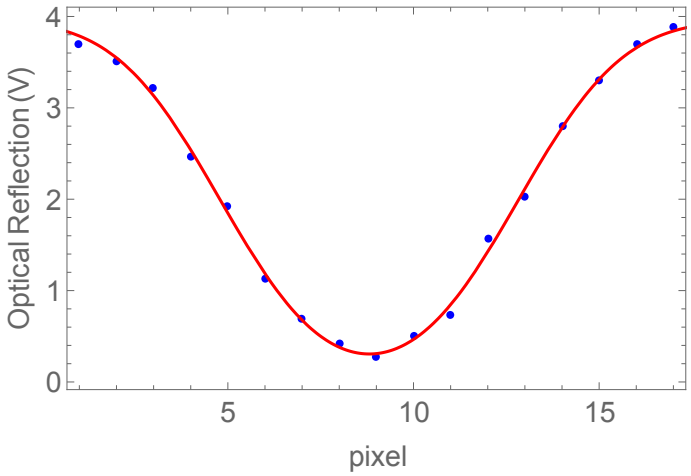

Figure 7.2: Fitting of the rectangular width from the optical reflection measurement against the 1µm teststructure (in pixel)

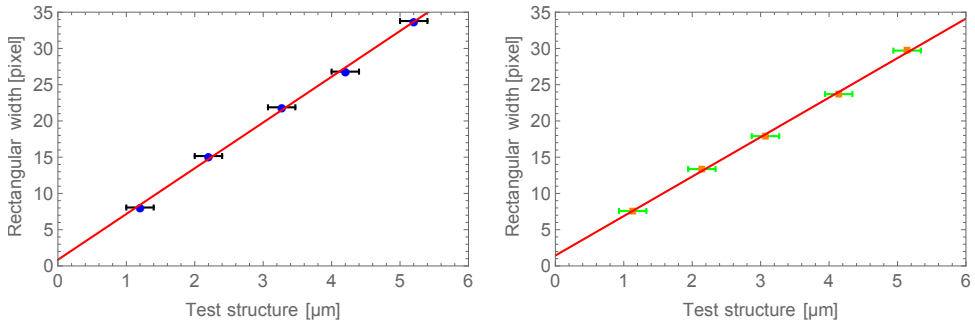

Figure 7.3: Plot of the fitted rectangular width against test structure width with vertical (left) and (right) horizontal test structure from 1 to 5 µm

The gradients were determined to be 0.184 ± 0.003 μm per pixel, 0.158 ± 0.004 μm per pixel for horizontal and vertical test structure, respectively. These values provide the direct conversion from pixel to the actual step size, hence we can estimate the minimum beam spot size with the previously fitted beam spot width in pixels. The final measured beam spot width are shown in fig. 7.4.

To sum up, both the vertical and horizontal beam spot size possess a very

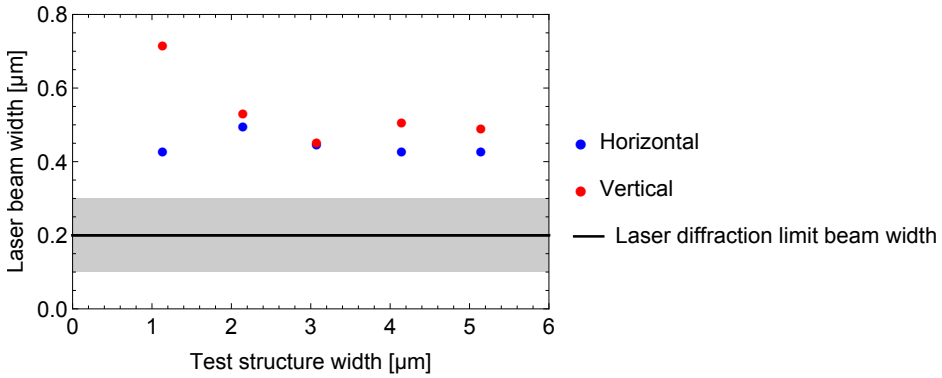

Figure 7.4: Calibrated beam spot size with horizontal and vertical test structure

small width up to $(0.492 \pm 0.030)\ \mu m$, this indicates that the laser can resolve the structure up to a very high spatial resolution, with minimum resolution defined by the beam spot size. Furthermore, we can also compare our measurement with the diffraction limited beam size, see eq. (7.1). The diffraction limited beam spot was then estimated to be $(0.2 \pm 0.1)\ \mu m$, close to half of our calibrated beam spot size, this indicates that we have obtained a high precision for the scan resolution.

$$d = 1.22\frac{\lambda}{NA} \tag{7.1}$$

where λ is the wavelength of the laser, and the numerical aperture (NA) was measured to be 0.29 ± 0.1.

7.2 Measurement of the spacial dependence of the photo-response: Labview automatization

An important aspect of the project consisted in the conception of a Labview program that would allow to perform measurements involving the dependence in the position of the laser in an automatic fashion, as it has already been evoked in section 3. The software running the Attocube SPN Scan Controller ASC500, called *Daisy*, does not directly allow us to define a path or a grid for the laser position to perform microwave measurements step after step. An interface between Daisy and Labview has to be used. In this section, we present the general idea behind running Daisy via Labview, and three different programs that were written with this goal, namely the *Step-by-Step Stepper*, the *Step-by-Step Scanner* and the *Pathmode Scanner*. The latter was chosen to be added into the SweepSpot software in order to perform in a convenient way laser position dependence measurements.

7.2.1 Running the Attocube ASC500 software with Labview

As it is explained in the ASC500 User Manual [14], a Remote Control package is provided to allow running basic Daisy functionalities via Labview. This provides the obvious advantage that a Labview program can perform other tasks, such as a microwave measurement, while using Daisy functionalities, such as the Scanner.

The two main components of the Remote Control package are a library, `ASC500_Wrapper.dll`, which allows using the Daisy functionalities in Labview and a set of Virtual Instruments (VIs) that are functions of the Daisy software that can be used in Labview. Some of these include preparing the laser at a certain position, performing a scan, etc. Therefore, the library must be loaded each time an ASC500 VI is used[1] to make the program run correctly. The connection between the ASC500 and Labview is made via a server. Alternatively, it is much more convenient to run Labview and Daisy in parallel, so that each parameter appearing in Daisy can be modified via Labview and vice-versa. This is sketched on figure 7.5.

If Daisy is opened in parallel, an important point is to keep the same channel definitions in Labview as in Daisy (e.g. Channel 10 is the Lineview), otherwise there can be interferences between Labview and Daisy preventing Daisy to run correctly.

We now have the main ingredients to implement VIs following our goal. Of the three VIs that will be presented in the next subsections, only the Pathmode Scanner has been of actual use. Nevertheless, since it can be

[1] On the QUDEV70 computer, it can be found in `D:\AttoCube\ASC500 Software\ASC500 Remote Control`

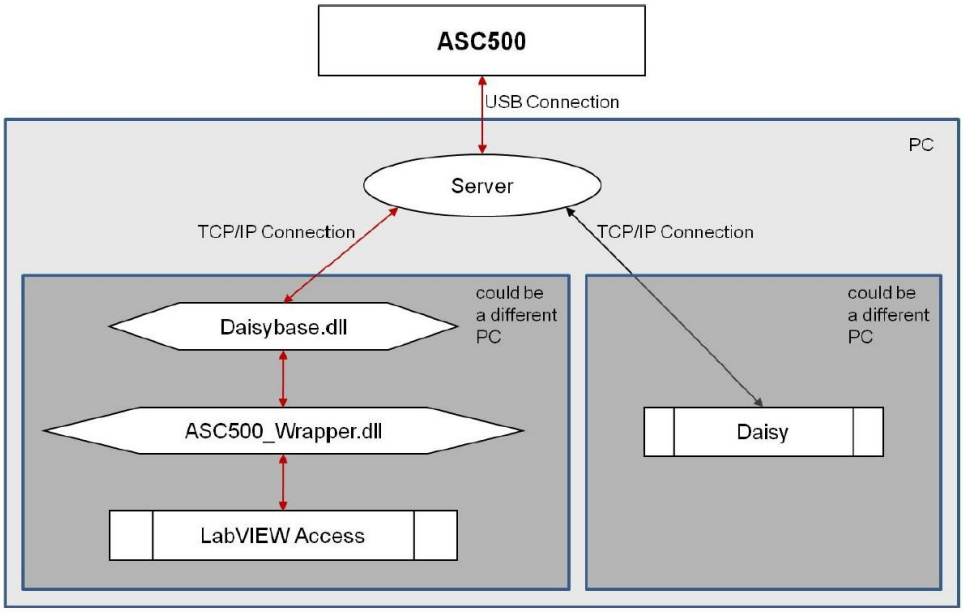

Figure 7.5: Sketch of the interface between the ASC500 and Labview [14].

of some interest for other applications to know that there are also other scanners that have been implemented in the frame of this thesis, we will introduce them all. All the VIs can be found on the `DaisySweep` folder on the QUDEV70 computer desktop.

7.2.2 The Step-by-step Stepper

The first VI that has been implemented to perform the step by step scan is the `StepByStepStepper.vi`. The idea behind this scanner is to use the Stepper functionality of Daisy, which is useful for larger scans, of a range up to 1-2 mm. The conception is the following, as sketched on figure 7.6:

1. Define a grid of points to scan over, with a certain origin, range and pixel size, to prepare the scan. The two following steps are then performed iteratively over all the grid.
2. Move the laser at the next point of the grid using the ASC500 steppers.
3. Read out the reflection intensity using the Lineview.

This results in a scan that gives the reflection amplitude as a function of position, the actual x and y position of the laser and the error with respect to the value that was set. The two-dimensional picture we get for the reflection

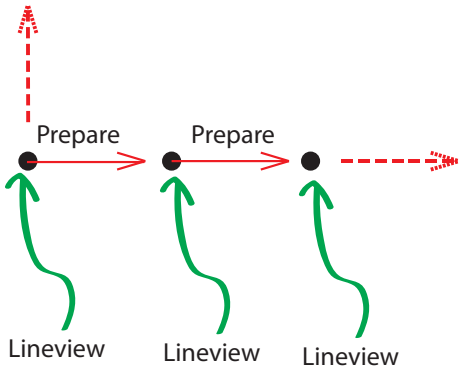

Figure 7.6: Working principle of the Step-by-step Stepper.

amplitude is of the same quality as the scan made on Daisy with the Stepper, but the time needed to perform the measurement is a bit higher.

The major drawback of this VI in the frame of our thesis is the fact that the resolution of the picture is not good enough if we want to resolve precisely structures that have a width of 1μm. We therefore must turn ourselves towards the ASC500 functionality that is more adapted to this range: the Scanner.

7.2.3 The Step-by-step Scanner

In order to create a scanner that can resolve inductor lines of 1μm, the ASC500 scanner functionality should be used. This is why in a second time such a VI, the `StepByStepScanner2.vi`, has been implemented. The trick which is used is to perform single-pixel scans at each point of the scanning grid. Concretely, the idea is the following, as sketched on figure 7.7:

1. Define a grid of points to scan over, with a certain origin, range and pixel size.
2. Move at the origin using the Stepper.
3. Make a single pixel scan at the first point, to actually move the laser at the given position.
4. Retrieve the reflection intensity using the Lineview.
5. Do it repeatedly for all the points of the grid.

Since this is not a "natural" way to use the scanner functionality, several problems arose in this implementation. A problem is that at each individual scan, the Z position correction is reinitialized to zero by the VI. A solution is to set it back to its correct value at each step, but since the laser is "shaking"

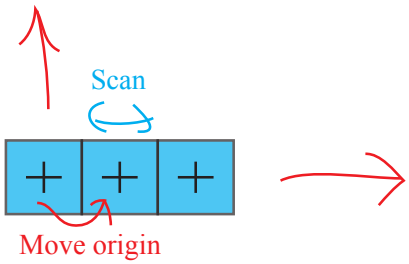

Figure 7.7: Working principle of the Step-by-step Scanner.

in Z direction, the resulting image is terribly blurred. Waiting for the laser to stabilize at each point dramatically increases the duration of the scan. A solution is to put the laser at an acceptable Z position with the stepper before the scan, but the picture then cannot be optimally focused. A more decisive drawback is the fact that the quality of the picture is clearly worse than with the original scanner. This is probably due to the fact that the laser is not set as precisely to the origin of the scan as to the points reached during the scan.

7.2.4 The Pathmode Scanner

To make a better use of the scanner functionality, a way to interrupt the scan in a "natural" way has to be found. It turns out that there is a functionality in Daisy called the *Pathmode*. It allows to define a path or a grid for the scanner and to stop at each scanning point, waiting for an external signal or a manual signal, called *handshake*. This leads to our final implementation of a Labview VI, namely `PathmodeScanner.vi`. As sketched on figure 7.8, the conception is the following:

1. Prepare the laser at the origin, using the Stepper.
2. Define a path or grid that gives all the points to scan over
3. Enable the external handshake mode
4. Retrieve the reflection amplitude at each point, using the Lineview. To move to the next point, simply virtually press the Manual Handshake button via Labview.

This implementation allows to make measurements that are as precise as the ones that are made with Daisy's scanner in an acceptable time, as can be seen on figure 7.9. We therefore achieved our goal to create a Labview VI that encompasses all the functionalities of the scanner but allows to perform other measurements at each point of the scan. At this time a drawback of the

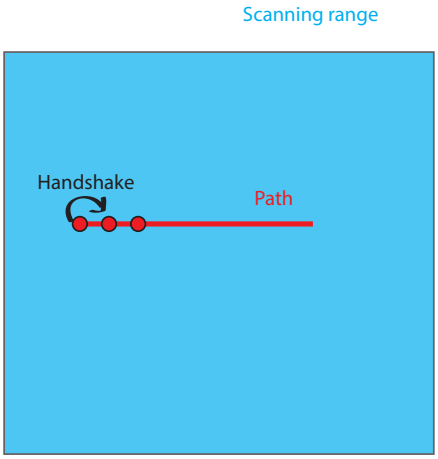

Figure 7.8: Working principle of the Pathmode Scanner.

Pathmode Scanner is the impossibility to properly define two-dimensional scanning grids. Nevertheless, in order to perform photo-response measurements, simple paths going through conducting lines are sufficient. Therefore, the Pathmode scanner has been chosen to perform the spatial dependence measurement and to be included in the main software SweepSpot.

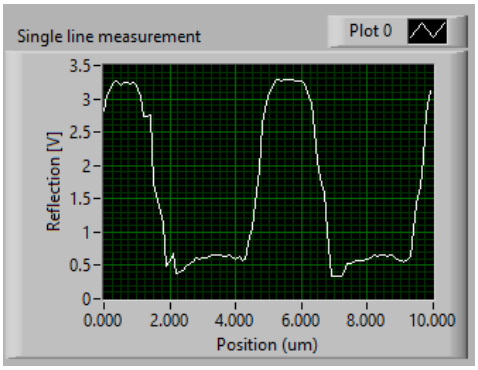

Figure 7.9: Reflection amplitude as a function of the laser position going through a 3 µm inductor line. The range is 10 µm. The time that this measurement took was 33.2 s.

Pathmode Scanner user manual

In an actual experiment using the implementation of the Pathmode VI into a microwave measurement software, the Pathmode Scanner can actually be

useful to determine before the measurement whether the defined path goes through the desired structure. Therefore, we finally describe in more detail how to *use* the `PathmodeScanner.vi`. The overview of the VI can be seen on figure 7.10.

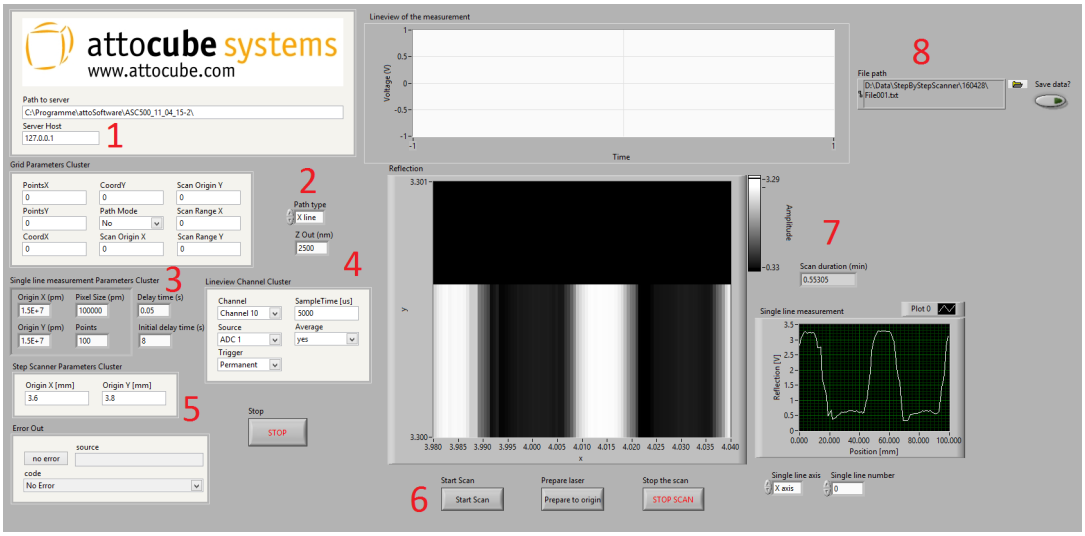

Figure 7.10: Front panel of the Pathmode Scanner VI. For a complete description please see the body text.

To find the VI, go to the QUDEV70 computer desktop and open the folder `DaisySweep`. On the front panel, a server to connect to ASC500 must be specified (1). In the case Daisy is running on the same computer, just enter the localhost IP address 127.0.0.1. Then, the path type (grid or path in X or Y direction) as well as the correction to the Z position should be specified (2). Then, the parameters of the path are needed (3), such as the scanner origin, pixel size and number of points. Beware that there should be less than 200 points defined (it is the limit of the Pathmode), otherwise the scanner will start to behave unexpectedly. The initial delay time allows for the laser to reach the first point (10s are typically enough) and the delay time is the minimum time between two handshakes, to avoid handshaking before the laser has actually reached the desired point. To read out the reflection amplitude, Lineview is used and some parameters should be set (4). The

correct settings for the Lineview are given in table 7.1.

Channel	Source	Trigger
10	ADC1	Permanent

Table 7.1: Correct parameters for the Lineview.

To move the laser to an absolute origin using the stepper, specify Origin X/Y and press the "Prepare to origin" button (5). Finally, the scan can be started by pushing the "Start Scan" button (6). The results are shown live on the Lineview and on the two- and one-dimensional plots after the measurement has been completed (7). The one-dimensional plot allows to get a single measurement line out of the two-dimensional plot. Finally, the data can be saved by pushing the "Save data?" button before starting the scan (8).

7.2.5 Inclusion of the Pathmode Scanner into SweepSpot

Until now, we have a Pathmode Scanner VI that is able to do reflection amplitude measurements. This is a nice sign that the VI works properly, but at the end of the day, what we want to perform are microwave measurements. We therefore need to include our Pathmode Scanner into a software which is able to perform such measurements. The software *SweepSpot* has been chosen[2]. With the help of Simon Storz, whose Master thesis is dedicated to designing SweepSpot, a version of the Pathmode Scanner that does not measure the Lineview has been added to the main software. The idea is simply to add it as an additional instrument that allows to create a new measurement axis: the laser position. At each iteration, SweepSpot does one Manual Handshake to go to the next laser position and performs the microwave measurement. More precisely, the Pathmode Scanner has been splitted into three parts:

1. One SubVI in `Prepare Sweep.vi` that sets all the right parameters for the laser motion.
2. One SubVI in `Spot.vi` that makes the laser move to the next point before each measurement, simply virtually pressing the Manual Handshake button.
3. One SubVI in `Motion reversal.vi` that makes the clean-up (empty the path, stop the scanner, shut down the connection to the server).

[2]For an introduction to SweepSpot, please see https://qudevwiki.phys.ethz.ch/index.php/SweepSpot or Simon's Master thesis.

Sweeping over the laser position with SweepSpot

To make it possible for further generations to easily use the laser position sweep dimension on SweepSpot, we here briefly explain how to do it. First, open `SweepSpot frontend.vi`, making sure to run Daisy in parallel and to load the Remote Control library while opening the VI. Then, on the front panel, first go to the Sweep Controls and Sweep Dimensions, see figure 7.11, and set the initial parameters such as the origin, the pixel size, the number of points and the path type (X/Y path or grid[3]). Beware that the positions are defined in pm. Also add the laser position as a sweep dimension to sweep over it.

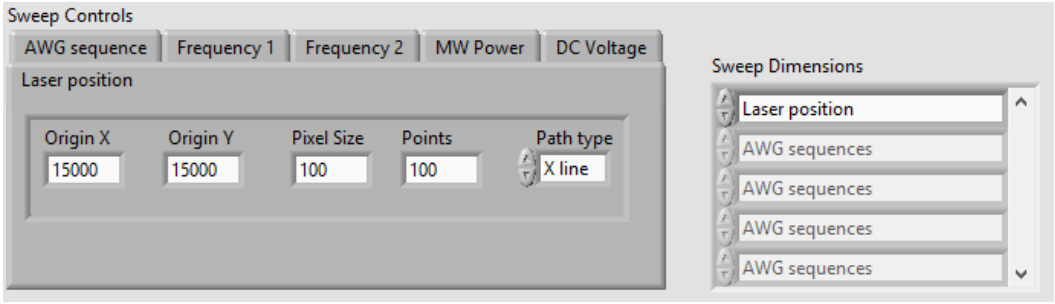

Figure 7.11: Sweep Controls and Sweep Dimensions on SweepSpot frontend's front panel

Finally, there are also the Instrument Settings to set, as shown on figure 7.12. Z Out, in nm, is the correction for the laser position on the Z axis and the delay time in seconds is the time that is taken between two handshakes to avoid "handshaking" too fast.

[3] As mentioned before, the grid functionality does not work properly by the time this thesis is written.

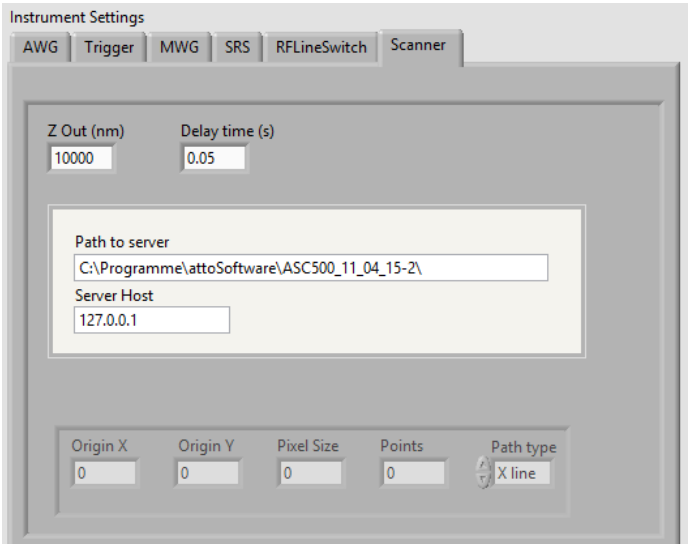

Figure 7.12: Instrument Settings on SweepSpot frontend's front panel

7.3 FPGA PR measurement of 1 μm monomer with microwave and laser dependence

In this section, the microwave and laser power dependence in a focused laser regime were studied. Varying the microwave and laser power allows one to understand the effects of changing laser and microwave power on photo response, and to optimise the experimental parameter for more precise measurements. We performed measurement here with the static photo response measurement, where each measurements were performed by comparing the change in reflected voltage ΔV_{out} with laser on and the laser turned off across a large frequency range.

Microwave power dependence of PR

One of the main goal of the current experiment is to do LSM under the quantum limited microwave power regime. Therefore, it is interesting to investigate the effect of microwave power on the photo response. From a previous master thesis by J.Chen, it was shown [7] that under a small laser perturbation, i.e. a defocused laser, the small induced change in kinetic inductance and resistance would lead to the square root dependence between the reflected microwave power and the photo response eq. (7.2).

$$PR \propto \Delta V_{out} = \frac{1}{2}\sqrt{\frac{R}{P}}\Delta P \propto P^{\frac{1}{2}} \tag{7.2}$$

where ΔV_{out} is the induced change in reflected signal, P is the microwave power and ΔP is the change in reflected power.
The microwave dependence of PR was measured with a focused laser beam at temperature of 3K, RF power sweeping from -102 dBm to -116 dBm at the sample. In fig. 7.13, the photo response clearly exhibited no square root dependence as opposed to the case in the defocused laser regime, fluctuations in measurements could be caused by random piezo movement of the focused laser beam spot, falling into the gaps between the inductor lines.

The laser induced change in resonance frequency and intrinsic loss were included at fig. 7.14. $-\Delta\nu_0$ and $-\Delta\gamma$ were found to be independent of the microwave power, which matches the prediction from theory [7].

Laser power Dependence of PR

Photons impinging onto the inductors indirectly break Cooper pairs locally, increasing the laser power would excite more quasiparticles, thereby changing the LC resonator properties such as resonance frequency ν_0 and the intrinsic decay width γ. In order to perform quantised LSM, laser induced heating at high laser power should be avoided, whereas at low laser power,

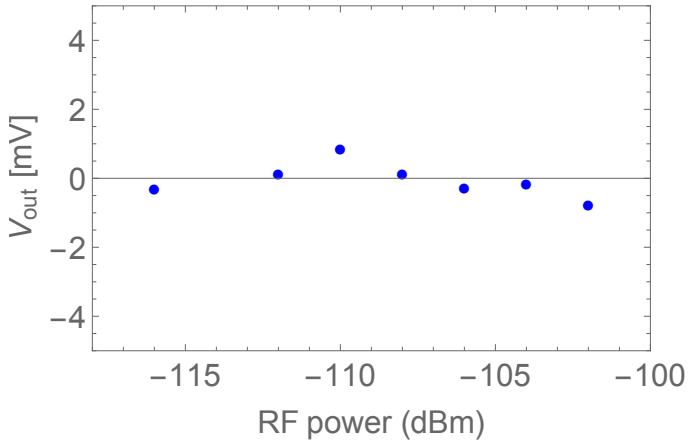

Figure 7.13: Microwave power dependence of photo response swept from -102 to -116 dBm at 10.66μW focused laser at sample and 4K temperature. The anomalous point at -114 dBm was removed due to poor fitting

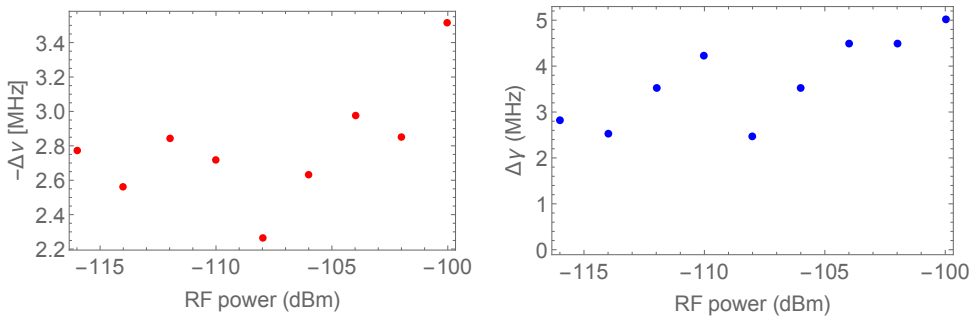

Figure 7.14: Laser induced change for microwave power swept from -102 to -116 dBm with focused laser power at 10.66μW (a) Left: change of resonance frequency $-\Delta\nu_0$ (b) Right: change of intrinsic decay width $-\Delta\gamma$.

the effect of thermal fluctuation is comparable to the laser induced change, causing imprecision in measurement. Therefore, compromise between two effects must be reached to operate in the quantised LSM regime.

Figure 7.15 shows the Log plot of the laser power dependence of photo response measured with RF power of -100dBm at 3K with focused laser beam. The plot shows a clear transition of laser power regime at around $10\mu W$ where above which the photo response becomes much stronger. In contrast to a highly defocused beam , it is not possible for a focused laser beam to break all the Cooper pairs locally, hence no saturation of PR was found [7].

In fig. 7.16(a) and fig. 7.16(b), the change in resonance frequency $-\Delta\nu_0$ and intrinsic decay width $\Delta\gamma$ both demonstrate exponential growth relationship

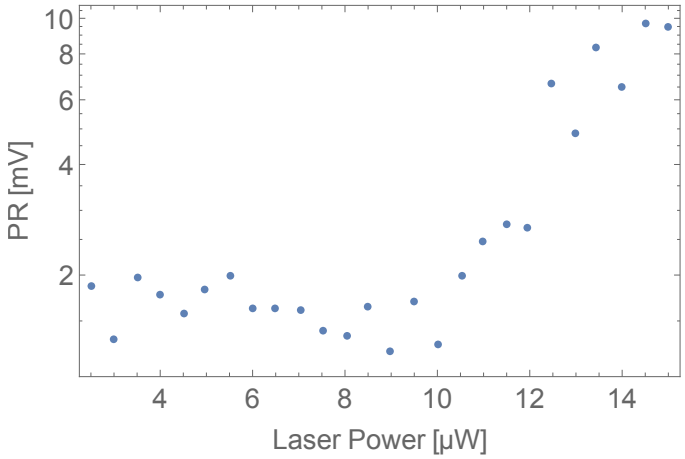

Figure 7.15: Laser power dependence of the photo response swept from laser power of 2μW to 15μW measured with RF power of -100dBm at 4K

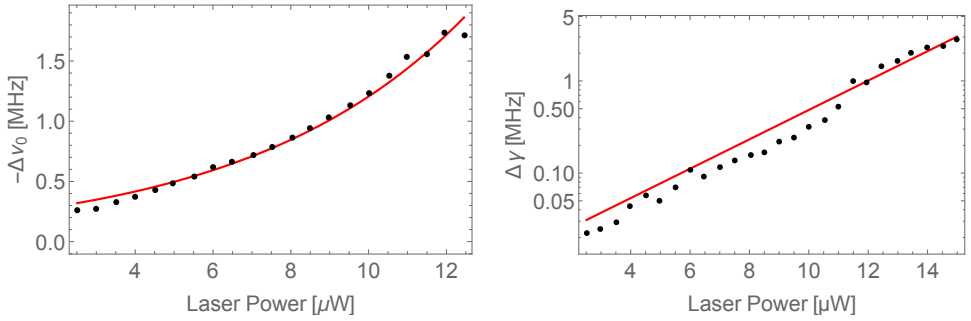

Figure 7.16: Laser induced change for laser power swept from 0 to 15 μW with focused laser power at -100dBm RF power, 3K (a) Left: change of resonance frequency $-\Delta\nu_0$ (b) Right: Log plot change of the intrinsic decay width $\Delta\gamma$.

with the increasing laser power. The plots were fitted with an exponential model, $y = ae^{bx}$, for $-\delta\nu_0$ and $\delta\gamma$, good fitting were found with the following coefficients, $a = 0.0123$ MHz, $b = 0.367\ \mu W^{-1}$ and $a = 0.2048$ MHz, $b = 0.177\ \mu W^{-1}$. For the change in resonance frequency and intrinsic decay width, it was observed that the gradient remains small at low laser power regime. Whereas, at the high power regime, the steeper gradient indicates the resonance shifted to the lower frequency slowly and broadens as the laser power is ramped up.
To conclude, we have observed similar trend of PR against laser power and microwave power as one observed in section 5.2. The strong exponential growth of $-\delta\gamma$ and $\delta\nu_0$ further confirm the weak coupling and large PR of the 1 μm monomer.

Bibliography

[1] I. Walmsley, "Quantum technology shines bright," *NQIT*, 2015.

[2] R. P. Feynman, "Simulating physics with computers," *International journal of theoretical physics*, vol. 21, no. 6, pp. 467–488, 1982.

[3] H. S. Newman and J. Culbertson, "Measurement of the current density distribution in high temperature superconducting microstrip by means of kinetic inductance photo response," *Microwave and Optical technology letters,*, vol. 6, p. 13, 1993.

[4] A. P. Zhuravel, "Unconventional rf photoresponse from a superconducting spiral resonator," *Phy. Rev. B*, 2012.

[5] L. P. K. Day, H. G., "A broadband superconducting detector suitable for use in large arrays," *Nature*, vol. 425, no. 817-821, 2003.

[6] S. M. A. A. P. Zhuravel and A. V. Ustinov, "Measurement of local reactive and resistive photoresponse of a superconducting microwave device," *Applied physics letter*, vol. 88, p. 212503, 2006.

[7] J. Chen, "Laser scanning microscopy of microwave superconducting lumped element resonators," *Quantum Device Group*, 2015.

[8] R. P. Budoyo, "Effects of nonequilibrium quasiparticles in a thin-film superconducting microwave resonator under optical illumination," *Phys. Rev. B*, 2016.

[9] A. Bargerbos, "Coupled lumped-element resonators with periodic boundary conditions," *Quantum Device Group*, 2015.

[10] L. S. Bishop, *Circuit Quantum Electrodynamics*. PhD thesis, Yale University, 2010.

[11] Antonio Rubio Abadal, "Josephson Parametric Amplifiers with Lumped-element Coupled Resonators," *ETH Zurich*, 2015.

[12] A. R. A. Anton Potocnik, "Towards input-output theory for an array of coupled lumped-element resonators," *ETH Quantum Device Group*, 2015.

[13] S. Gyger, "Improved measurement method for spatial-dependence photo response," *ETH Quantum Device Group, Physics Department*, 2016.

[14] Attocube, *ASC500 Remote Control with Labview*, March 2011.

ETH

Eidgenössische Technische Hochschule Zürich
Swiss Federal Institute of Technology Zurich

Declaration of originality

The signed declaration of originality is a component of every semester paper, Bachelor's thesis, Master's thesis and any other degree paper undertaken during the course of studies, including the respective electronic versions.

Lecturers may also require a declaration of originality for other written papers compiled for their courses.

I hereby confirm that I am the sole author of the written work here enclosed and that I have compiled it in my own words. Parts excepted are corrections of form and content by the supervisor.

Title of work (in block letters):

IMPROVED LASER SCANNING MICROSCOPY METHOD AND CHARACTERIZATION OF ANNULAR LUMPED ELEMENT RESONATORS

Authored by (in block letters):

For papers written by groups the names of all authors are required.

Name(s):	**First name(s):**
Bettermann	Oscar
Ngai	Chun Tat

With my signature I confirm that

- I have committed none of the forms of plagiarism described in the 'Citation etiquette' information sheet.
- I have documented all methods, data and processes truthfully.
- I have not manipulated any data.
- I have mentioned all persons who were significant facilitators of the work.

I am aware that the work may be screened electronically for plagiarism.

Place, date	**Signature(s)**
Zurich, 31.10.2016	

5th Nov, 2016

For papers written by groups the names of all authors are required. Their signatures collectively guarantee the entire content of the written paper.